Chapter 4
Use of GNSS Tropospheric Products for High-Resolution, Rapid-Update NWP and Severe Weather Forecasting (Working Group 2)

Check for updates

S. de Haan, E. Pottiaux, J. Sánchez-Arriola, M. Bender, J. Berckmans, H. Brenot, C. Bruyninx, L. De Cruz, G. Dick, N. Dymarska, K. Eben, G. Guerova, J. Jones, P. Krč, M. Lindskog, M. Mile, G. Möller, N. Penov, J. Resler, W. Rohm, M. Slavchev, K. Stoev, A. Stoycheva, E. Trzcina, and F. Zus

S. de Haan
Royal Netherlands Meteorological Institute, De Bilt, The Netherlands
e-mail: siebren.de.haan@knmi.nl

E. Pottiaux (✉) · C. Bruyninx
Royal Observatory of Belgium, Brussels, Belgium
e-mail: eric.pottiaux@oma.be; carine.bruyninx@oma.be

J. Sánchez-Arriola
AEMET, Santander, Spain
e-mail: jsancheza@aemet.es

M. Bender
Deutscher Wetterdienst, Offenbach, Germany
e-mail: michael.bender@dwd.de

J. Berckmans · L. De Cruz
Royal Meteorological Institute of Belgium, Brussels, Belgium
e-mail: julieb@meteo.be; lesley.decruz@meteo.be

H. Brenot
Royal Belgian Institute for Space Aeronomy, Uccle, Belgium
e-mail: hugues.brenot@oma.be

G. Dick
GFZ German Research Centre for Geosciences, Helmholtz Centre Potsdam, Potsdam, Germany
e-mail: dick@gfz-potsdam.de

N. Dymarska · G. Möller
Department of Geodesy and Geoinformation, TU Wien, Wien, Austria
e-mail: natalia.dymarska@geo.tuwien.ac.at; gregor.moeller@geo.tuwien.ac.at

K. Eben · P. Krč · J. Resler
Institute of Computer Science of the Czech Academy of Sciences, Prague, Czech Republic
e-mail: eben@cs.cas.cz; krc@cs.cas.cz; resler@cs.cas.cz

G. Guerova
Physics Faculty, Department of Meteorology and Geophysics, Sofia University "St. Kliment
Ohridski", Sofia, Bulgaria
e-mail: guerova@phys.uni-sofia.bg

J. Jones
Met Office, Exeter, UK
e-mail: jonathan.jones@metoffice.gov.uk

M. Lindskog
Swedish Meteorological and Hydrological Institute, Norrkoping, Sweden
e-mail: magnus.lindskog@smhi.se

M. Mile
Hungarian Meteorological Service, Budapest, Hungary
e-mail: mile.m@met.hu

N. Penov · K. Stoev (✉)
GNSS Meteorology Group Sofia University "St. Kliment Ohridski", Sofia, Bulgaria
e-mail: npenov@uni-sofia.bg; krasi@phys.uni-sofia.bg

W. Rohm · E. Trzcina
Institute of Geodesy and Geoinformatics, Wrocław University of Environmental and Life
Sciences, Wrocław, Poland
e-mail: witold.rohm@igig.up.wroc.pl; estera.trzcina@igig.up.wroc.pl

M. Slavchev · A. Stoycheva
National Institute of Meteorology and Hydrology, Sofia, Bulgaria
e-mail: martin.slavchev@meteo.bg; anastassia.stoycheva@meteo.bg

F. Zus
GFZ German Research Centre for Geosciences, Potsdam, Germany
e-mail: zusflo@gfz-potsdam.de

Abstract For more than a decade, GNSS-meteorology has been increasingly used operationally in Europe particularly for data assimilation in Numerical Weather Prediction (NWP) models, mainly thanks to the EIG EUMETNET GNSS Water Vapour Program (E-GVAP, 2005-today). As such, GNSS has become a well-established, mature observing technique for data assimilation applications. Over this period however, scientists and specialists in GNSS-meteorology noted the clear potential for enhancements and novelties in the domain. The work carried out by the COST Action ES1206 Working Group 2 members addressed these potential enhancements and novelties from the meteorological point of view, in collaboration with WG1. This included the establishment of discussion channels with forecasters in order to determine which GNSS products would be best suited for their day-to-day operational requirements. Particular areas of interest include engaging more operational forecasters (e.g. use of meteorological case studies), especially for non-numerical nowcasting of severe weather, and getting more meteorological agencies to assimilate GNSS products in regions of Europe where they were not yet/well exploited. It also included the development of the techniques and tools

necessary to benefit from the brand new products developed by the Action WG1 and WG2 members, namely real-time GNSS tropospheric products for rapid-cycle NWP and non-numerical nowcasting, data assimilation of horizontal tropospheric gradients and tropospheric slant delays as well as tomographic products. Finally, the work carried out by the WG2 members brought operational improvements through dialog, transfer of knowledge, and standardisation (e.g. the new standardized tropo-SINEX format or the development of assimilation operators). The major WG2 outcomes are discussed in this Chapter.

4.1 Introduction

S. de Haan
Royal Netherlands Meteorological Institute, De Bilt, The Netherlands
e-mail: siebren.de.haan@knmi.nl

E. Pottiaux
Royal Observatory of Belgium, Brussels, Belgium
e-mail: eric.pottiaux@oma.be

J. Jones
Met Office, Exeter, UK
e-mail: jonathan.jones@metoffice.gov.uk

GNSS4SWEC Working Group 2 (WG2) was established primarily to define and improve the use of GNSS tropospheric products for high-resolution, rapid-update numerical (i.e. NWP) and for non-numerical (e.g. forecaster visualisation) nowcasting, with a specific focus on severe weather events. Historically, the primary user of GNSS-meteorological outputs (i.e. ZTD and IWV) were the NWP community, using ZTD for assimilation into local and regional NWP models. Whilst the NWP community still represents a very important user of GNSS products, other users are becoming more evident such as the forecaster and climate communities, and it is an overall aim of this COST Action to better engage these communities. With regards to WG2, forecasters at a number of national meteorological and hydrological agencies were engaged to publicise the usefulness of GNSS-derived IWV fields (images and animations) in certain conditions, and also to better understand the role and requirements of the forecaster when considering future products.

As well as assessing the use of the more traditional GNSS-tropospheric products (i.e. ZTD and IWV), WG2 also looks to assess the impact of more advanced tropospheric products developed by WG1 such as slants and gradients in NWP schemes, and also assesses the benefits and status of GNSS-tomography.

A number of work packages were defined to more efficiently organise the activity in the different fields. The main areas of focus were:

WP 2.1 Non-numerical Nowcasting (Sect. 4.2)

- Review and exchange tools and methods for non-numerical GNSS nowcasting.
- Assess the benefit of new/enhance GNSS products (real-time, gradients, slants etc.) for non-numerical nowcasting.

- Organize detailed analyses of special case studies by non-numerical nowcasting (fog, foehn, precipitation etc.), and to establish a database of severe weather case studies that can be re-used.
- Draw recommendations for operational GNSS nowcasting.

WP 2.2 Numerical Nowcasting and NWP Assimilation (Sect. 4.3)

- Develop, validate and exchange methods for the initialization of NWP models using new/enhanced operational GNSS tropospheric products (e.g. gradients and slants), and for use in nowcasting.
- Evaluate and validate the information content of the enhanced, new products provided by WG1, such as gradients and slant delays (determine error sources, correlations etc.).
- Assess the benefit of multi-GNSS tropospheric products to NWP and severe weather forecasting.

WP 2.3 Tomography (Sect. 4.4)

- Review the status of tomography w.r.t. nowcasting and NWP data assimilation.
- Organise inter-comparison and validate tomography products.
- Organise a specific tomography case study.
- Identify tomography products capability in term of requirement for NWP and nowcasting.
- Develop operational tomography products and evaluate them.

WP 2.4 Benchmark and Case Study Databases (Sect. 4.5)

- Define and generate specific benchmark datasets in the form of GNSS observations, alternative water vapour and refractivity observations and NWP products, for test, assessment, and validation
- Establish a database with severe weather case studies (data, documentation etc.).
- Establish a database with meteorological data to enhance real-time GNSS positioning.

WP 2.5 ZTD2IWV Conversion (Sect. 4.6)

- Develop, validate and exchange methods to convert between ZTD and IWV.

4.2   Non-numerical Nowcasting

4.2.1   *Investigation of Fog in Bulgaria Using GNSS Tropospheric Products*[1]

A. Stoycheva
National Institute of Meteorology and Hydrology, Sofia, Bulgaria
e-mail: anastassia.stoycheva@meteo.bg

---

[1]Parts from this section were previously published in Stoycheva et al. (2017) and Stoycheva and Guerova (2015).

N. Penov
Sofia University "St. Kliment Ohridski", Sofia, Bulgaria
e-mail: npenov@uni-sofia.bg

G. Guerova
Physics Faculty, Department of Meteorology and Geophysics, Sofia University "St. Kliment Ohridski", Sofia, Bulgaria
e-mail: guerova@phys.uni-sofia.bg

Despite the continuous improvement of weather prediction fog diagnosis and forecasting remains a challenge with large economic losses for public services and in particular aviation where the cost of flight delays and re-scheduling is estimated to hundreds million euros per year. Today operational fog forecasting is mainly done with "in-house" developed tools. The aim of this work is to investigate the benefit of GNSS tropospheric products in operational fog forecasting in Bulgaria.

Three Fog Case Studies

Fog is low level phenomenon caused by suspended in the air water droplets resulting in visibility below 1000 m. Typical fog conditions for Bulgaria are anti-cyclonic weather with surface: (1) relative humidity over 90–95%, (2) light wind (below 2 m/s) and (3) temperature in the range ± 5 °C. Presented are three case studies of fog development and dissipation in three regions of Bulgaria namely: (1) Danubian plain (blue circles in Fig. 4.1), (2) Sofia valley (yellow circle in Fig. 4.1) and (3) Plovdiv plain (red circle in Fig. 4.1).
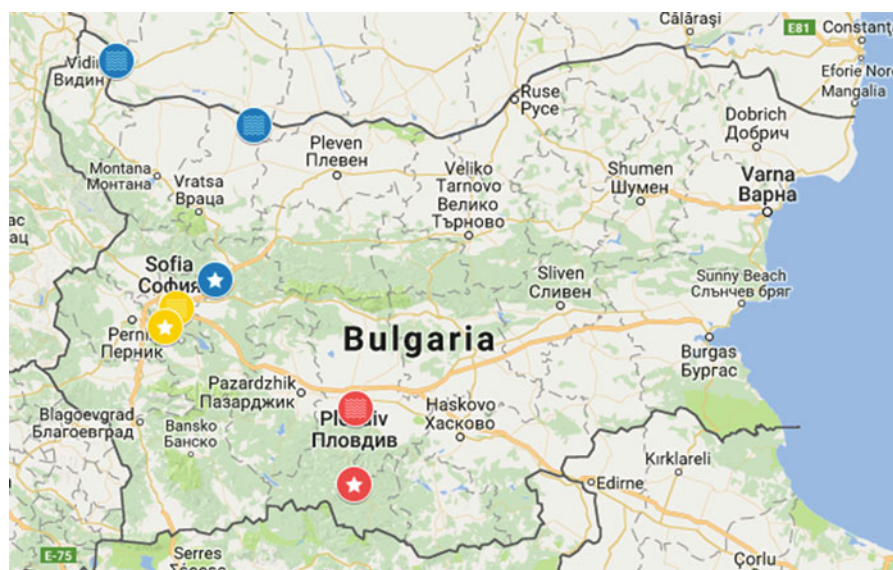

Fig. 4.1 Map of Bulgaria with marked locations of the case studies. Blue circles – Danubian plain fog (11–13 November 2012), yellow circles – Sofia valley fog (1–11 January 2014) and red circles – Plovdiv plain fog (13–16 December 2014)

Table 4.1 Names and altitude of the GNSS (column 2) and synop (column 3 and 4) stations used for case studies (column 1)

Case	GNSS stations	Synop low elevation station	Synop elevated station	Stability Index name
Case 1 11–13.11.2012	Vidin (31 m asl.)	Vidin (31 m asl.)	Murgash (1687 m asl.)	Vidin Stability Index (VSI)
	Oriahovo (29 m asl.)	Oriahovo (29 m asl.)		Oriahovo Stability Index (OSI)
Case 2 1–11.01.2014	Sofia (1164 m asl.)	Sofia (595 m asl.)	Cherni vrah (2292 m asl.)	Sofia Stability Index (SSI)
	Sredets (534 m asl.)			
Case 3 13–16.12.2014	Plovdiv (154 m asl.)	Plovdiv (154 m asl.)	Rozhen (1754 m asl.)	Plovdiv Stability Index (PSI)
	Rozhen (1754 m asl.)			

For each case IWV is derived from GNSS ZTD as described in Stoycheva et al. (2017). In addition, for case 2 the IWV difference is calculated by subtracting IWV from Sredec and Sofia. Equivalent potential temperature (EPT) is calculated following Holton (1972). Computed is also stability index (Stoycheva et al. 2017) using surface temperature observations at low level and elevated mountain synoptic station (marked with star in Fig. 4.1). In Table 4.1 are given the names and altitude of the GNSS (column 2) and synop (column 3 and 4) stations used for each case study.

Case Study 1: Danubian Plain

Presented in Stoycheva and Guerova (2015) are four fog case studies in the Danubian plain. Here is revisited the fog on 10–13 November 2012. In Fig. 4.2 are shown with grey bars the period with fog and with lines the EPT (dashed black), IWV (solid black) and stability indexes (solid red) for Vidin (VSI) and Oriahovo (OSI). The foggy periods in Vidin and Oriahovo differ and most notably the fog starts in Oriahovo 21 h earlier than in Vidin. Comparison of the diurnal cycle of EPT (Fig. 4.2a, b) on 11 November gives that a clear minimum is registered at 6:00 UTC in Oriahovo while at the same time in Vidin EPT remains constant for 6 h between 0:00 and 6:00 UTC. Interestingly, IWV has sharp increase in Vidin (9:00 UTC) while in Oriahovo it decreases (Fig. 4.2b and d). This can be explained with change of the air mass and in particular, IWV, being an integral characteristic of the troposphere, reflects the air mass transformation over time. The north-westerly air mass advection is confirmed in satellite images (not shown) and is registered 9 h later (18:00 UTC) in Oriahovo (Fig. 4.2d). The GNSS derived IWV give an indication of new air mass advection at altitude and the fog formation shows high sensitivity to upper level (1–2 km) advection. It is to be noted that VSI and OSI values are above 1 during the fog on 12–13 November and once the fog disperses drop. However, OSI is not sensitive for the visibility improvement on 12 November but the small IWV changes between 6:00 and 15:00 UTC give indication for transition between liquid
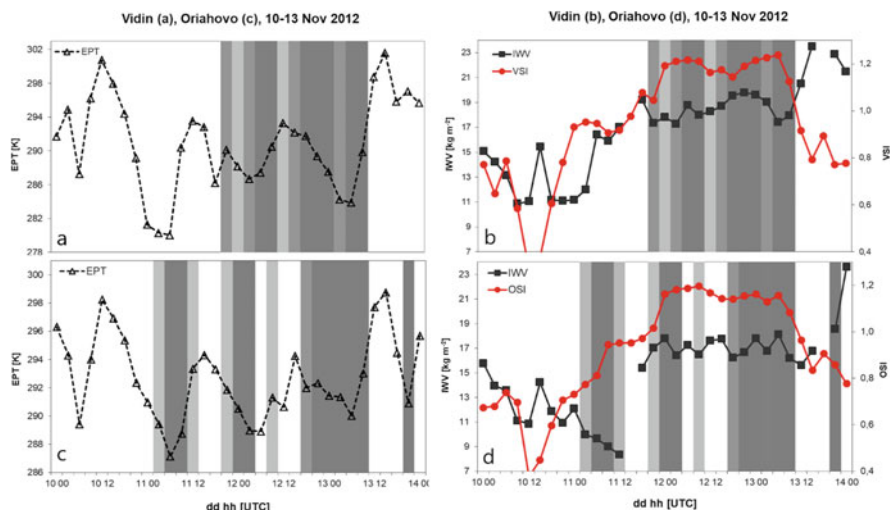
Fig. 4.2 Fog in Danubian plain 11–13 November 2012. The grey bars mark foggy periods. (**a**) and (**c**) EPT at Vidin and Oriahovo (dashed black line). (**b**) IWV in Vidin (solid black line) and VSI (solid red line). (**d**) IWV in Oriahovo (solid black line) and OSI (solid red line)

water and water vapour i.e. vapour increase with fog dispersion and drop with fog onset.

Case Study 2: Sofia Valley
Fog with duration under 24 h is mainly radiation fog with weak temperature inversion generally dispersed by noon. However, when a warm air is advected at the altitude in December and January the weak inversion transforms into powerful one with the fog layer strengthening day by day resulting in a prolonged fog lasting several days. The persistent fog (with duration over 24 h) is a result of interaction between surface, boundary layer and changes at the altitude, which makes prediction of visibility improvement or non-improvements around noon challenging. Here we review the presented in Stoycheva et al. (2017) case of persistent fog in Sofia valley in January 2014. Presented on Fig. 4.3 are the fog registrations in Sofia. The fog is separated in: (a) part I from 3 to 5 January (51 h), and (b) part II from 7 to 10 January (84 h). The part I and II are separated by 39 h with no fog (12:00 UTC on 5 January to 0:00 UTC on 7 January). As seen from Fig. 4.3a the EPT has a marked decrease for fog formation and increase with fog dispersion. In addition, it has a maximum during visibility improvement at 12:00 UTC on 3, 4, and 8 January. A transition of the air mass is recorded between fog part I and II, which is clearly visible in the sharp IWV increase from 10 to 18 kg/m^2 between 0:00 and 12:00 UTC on 5 January (black line on Fig. 4.3b). The Sofia Stability Index (SSI) has higher than 1 values for part II fog (red line in Fig. 4.3b). The SSI increase correlates well with the increase of horizontal visibilities in particular around midday on 8 and 9 January. With SSI drop below 0.8 at 15:00 UTC on 11 January the fog is dispersed. To study the IWV changes at the lower 600 m we compute a daily IWV difference (Sredec minus

Sofia). As seen in Fig. 4.3c the daily mean IWV difference (black dots) do not mark the days with fog but the within day variation of the IWV difference is smaller for the days with fog on 3, 4, 8, and 9 January (black whiskers in Fig. 4.3c). For comparison are given also the IWV differences from the Weather Research and Forecast (WRF) model. The model set-up is described in Stoycheva et al. (2017). The daily mean IWV from GNSS and WRF (red dots and whiskers in Fig. 4.3c) has correlation of 0.66 but the lower variance during fog is not reproduced in the model. As discussed in Stoycheva et al. (2017) the model does not simulate well the temperature inversion layers. The lack of adequate simulation of temperature profile and the inversion layer are the main reason for poor model skills in fog diagnoses and prognoses.

Case Study 3: Plovdiv Plain

In Plovdiv plain the fog is registered for 3-hour interval on 1 January and then for 33-hour period between 1 and 3 January 2013. Clearly seen from Fig. 4.4a is that EPT decreases with fog formation and increase with fog dispersion. The Plovdiv Stability Index (red line in Fig. 4.4b) has upward trend during fog formation (9 and 21:00 UTC on 1 January) and drops with fog dispersion (9:00 UTC on 3 January). The gap in the IWV data does not allow drawing major conclusions but the IWV decreases with fog formation with about 0.5 kg/m^2 between 18:00 and 21:00 UTC on 1 January and increases with fog dispersion by 1 kg/m^2 between 6:00 and 9:00 UTC on 3 January.

Conclusions

Investigation of fog formation and dispersion at different regions in Bulgaria shows that changes of the air mass are critical for timely fog prediction. The high temporal resolution of GNSS derived IWV plays a critical role in detecting local changes in the air mass and this makes it of particular interest for operational fog forecasting in particular for persistent fog. IWV decrease was found to result in fog formation while IWV increase to fog dispersion. We demonstrate the added value of IWV, equivalent potential temperature and stability index for studying fog. The results from this study are beneficial for development of a pilot transnational service exploiting GNSS tropospheric products to enhance the safety, the quality of life and environmental protection in the Balkan-Mediterranean region.

4.2.2   WRF Model Evaluation with GNSS IWV for Intense Precipitation Cases in Bulgaria

M. Slavchev
National Institute of Meteorology and Hydrology, Sofia, Bulgaria
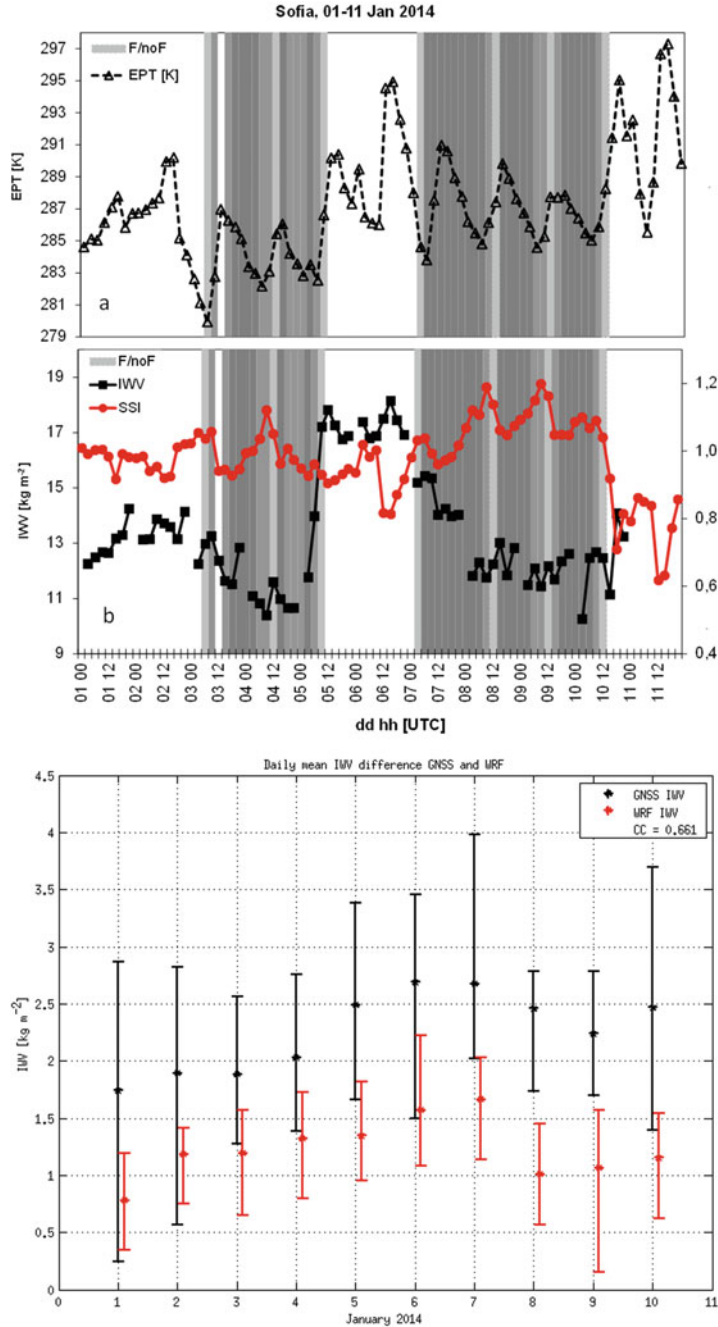e-mail: martin.slavchev@meteo.bg

Fig. 4.3 Persistent fog over Sofia valley 1–11 January 2014. With grey bars are marked fog periods. (**a**) EPT in Sofia (dashed black line). (**b**) IWV (solid black line) and Sofia Stability Index (SSI, solid red line). (**c**) daily mean IWV difference from GNSS (black dots and whiskers) and WRF model (red dots and whiskers)
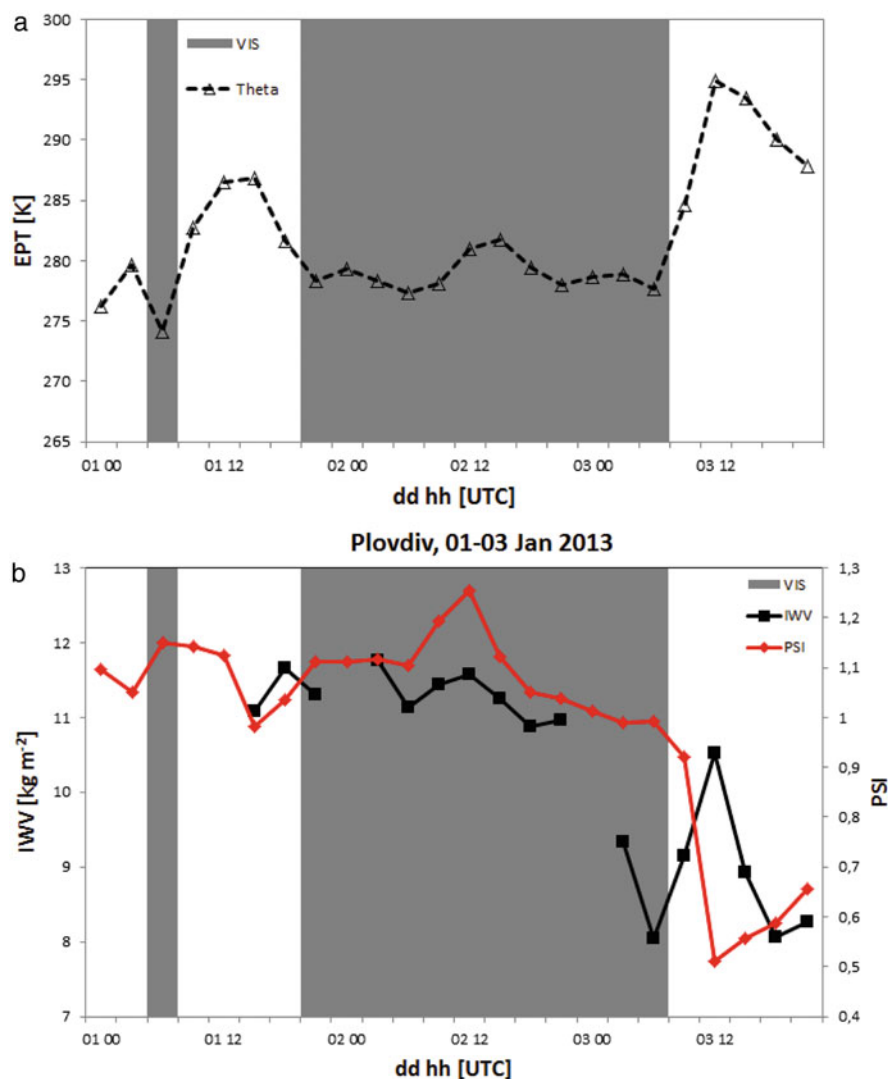
Fig. 4.4 Fog in Plovdiv plain 1–3 January 2013. Gray bars mark the fog periods. (**a**) EPT in Plovdiv (dashed black line). (**b**) IWV (solid black line) and Plovdiv Stability Index (PSI, solid red line)

G. Guerova
Physics Faculty, Department of Meteorology and Geophysics, Sofia University "St. Kliment Ohridski", Sofia, Bulgaria
e-mail: guerova@phys.uni-sofia.bg

Predicting formation and development of vigorous thunderstorms producing intense precipitation and hail is a complex process, which among other environmental conditions depend on accurate estimation of water vapour distribution in space and time. The goal of this work is to use GNSS derived IWV to evaluate the Weather Research and Forecasting (WRF) model skills for predicting the temporal and spatial variability during 20 intense precipitation events in Bulgaria during 2012.

In the last decade, nowcasting severe weather events is rapidly developing using both observations and Numerical Weather Prediction (NWP) models with high spatio-temporal variability and updates. However, prediction of correct time and location of precipitation is a known difficulty in particular in regions with complex topography like Bulgaria, which territory has 41% plateaus and hills (200–600 m asl.) and 20% low and medium-high mountains (600–1500 m asl.). In this work are selected and analysed 20 intense precipitation cases with frontal or convective origin. Conducted are 24-h forecast runs with WRF model v3.4.1 (http://www.wrf-model.org/index.php) and horizontal resolution 4 km and 44 vertical levels for Bulgaria (yellow rectangle in Fig. 4.5a. The used parameterization schemes are: (1) Double-moment 6 class scheme for microphysics, (2) Rapid Radiative Transfer Model/Dudhia scheme for long/short wave radiation, (3) Noah land surface model for land surface and (4) Yonsei University scheme for atmospheric boundary layer. Two experiments are performed by different cumulus parameterization set-up namely: (1) no parameterized convection (NCP) and (2) Kain-Fritsch (KF) cumulus parameterization. The IWV is derived for 30 GNSS stations from the Zenitgeo permanent network in Bulgaria (http://www.zenitgeo.com/about-us.html) and 80 from Greece (Fig. 4.5b). Schematic illustration of IWV computation from WRF and GNSS is given in Fig. 4.4. It is to be noted that the GNSS IWV is computed using surface pressure and temperature from the WRF model. Two
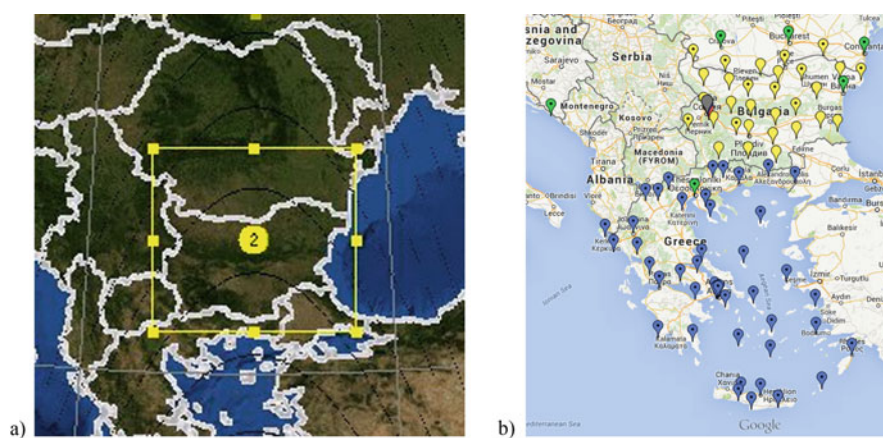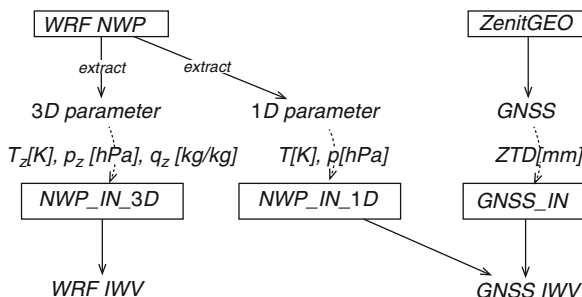

Fig. 4.5 (**a**) WRF model domain used in this work. (**b**) Map of South-east Europe with marled the GNSS stations in Bulgaria (yellow pointers) and Greece (blue pointers)

Fig. 4.6 IWV derivation from WRF and GNSS and WRF

dimensional (2D) IWV maps are produced via interpolation between the GNSS stations and application for altitude correction (Guerova 2013) (Fig. 4.6).

A detailed investigation of WRF model is conducted for the period from 8 to 28 May 2012 which covers 6 of the selected 20 cases. In Figs. 4.7a and b, IWV from GNSS (black dots) and two simulations namely WRF/KF (blue dots) and WRF/NCP (red dots) for Vidin (North-west Bulgaria) and Plovdiv (central Bulgaria) are shown. The WRF/KF simulation has consistently higher IWV, with mean of 31.0 and 31.4 kg/m^2, compared to the observed 28.8 and 28.0 kg/m^2. On the other side the WRF/NCP simulation tends to: (1) underestimate the IWV by about 3.3 and 2.6 kg/m^2, (2) has closer to the observed root mean square error (RMS) and (3) has higher correlation namely 0.83 and 0.78 for Vidin and Plovdiv respectively. For comparison correlation between GNSS and KF simulation is 0.74 and 0.56 for Vidin and Plovdiv correspondingly. Interestingly, there is IWV difference of 5.6 and 6.0 kg/m^2 between two model simulations, which shows that the WRF model has a high sensitivity to the convective processes during the selected period and also indicates potential for further improvement by assimilation of the GNSS IWV. It is to be noted that similar results are obtained for the remaining GNSS stations.

In Fig. 4.8a and b the IWV correlation coefficients for Plovdiv from GNSS and WRF/NCP for 10 cases with intense precipitation with mesoscale convective system origin (MSC) and 10 with frontal passage, respectively are shown. The visual inspection shows that the model has a better skill in simulating IWV for the frontal precipitation (Fig. 4.6b) with 7 out of 10 cases with correlation over 0.7. The correlation higher than 0.7 is registered for only 3 MCS cases.

On 27 June, intense MSC precipitation (74 mm) is registered between 9:00 and 15:00 UTC in northeast Bulgarian coast. From 2D GNSS IWV maps (Fig. 4.9) large variation in spatial distribution of IWV is seen with dry air mass covering only North Bulgaria at 00:00 UTC and then also South Bulgaria at 06:00 UTC. Within 6-hour period the IWV in South Bulgaria dropped by 10 kg/m^2 from 35 kg/m^2 at 00:00 UTC (Fig. 4.5a) to 25 kg/m^2 at 06 (Fig. 4.9c). The strong north-south gradient of IWV over the Balkan peninsula is seen also at 12:00 and 18:00 UTC (Fig. 4.9e and g). Large IWV gradient is confirmed by the SEVIRI-Meteosat maps in Fig. 4.9b, d, f and h (http://www.eumetrain.org/eport/tooltip/euro/sphr_tpw.html).

Evaluation of WRF model skills in IWV simulation of 20 intense precipitation cases in Bulgaria show: (1) high sensitivity to the selection of the convective scheme
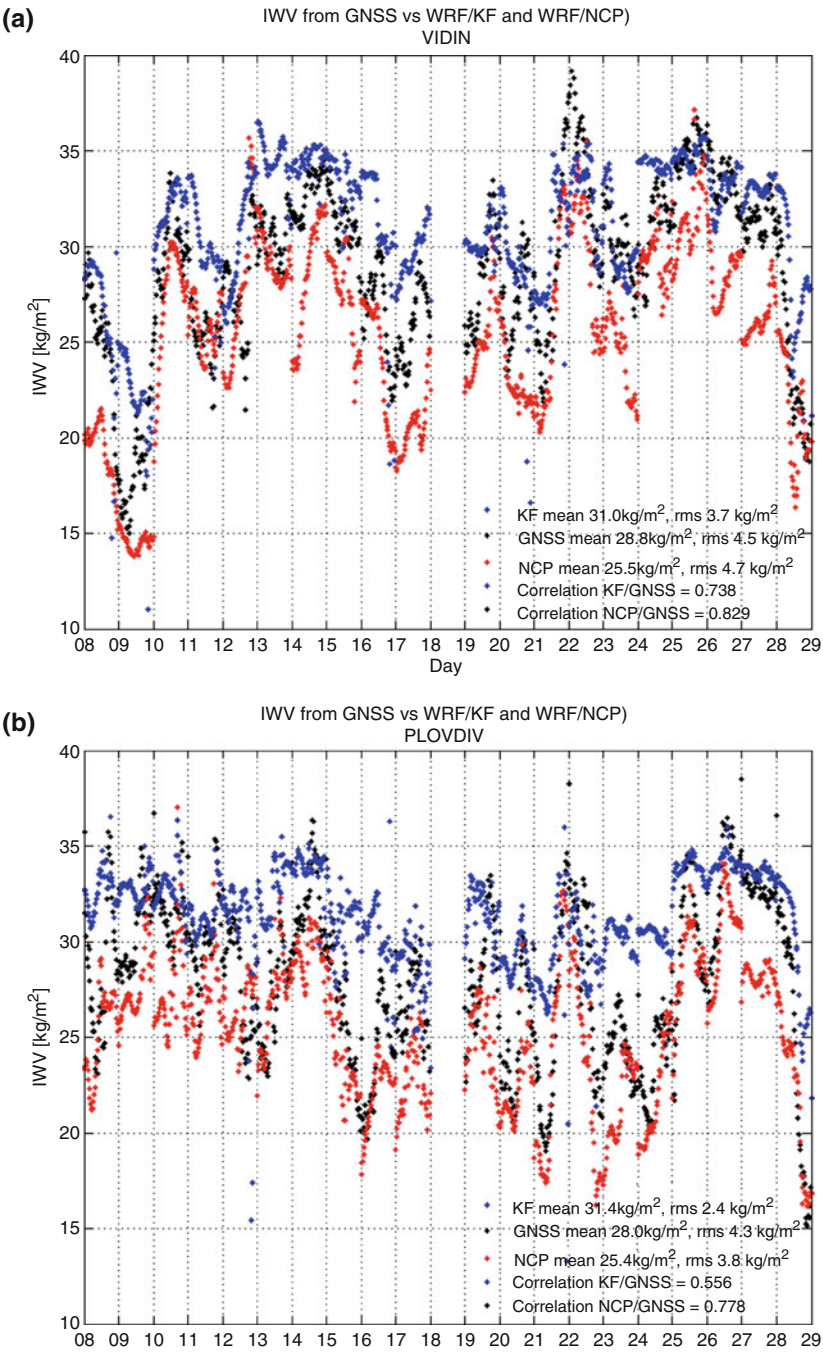
Fig. 4.7 IWV GNSS vs WRF/KF and WRF/NCP for: (**a**) Vidin and (**b**) Plovdiv 8–28 May 2012
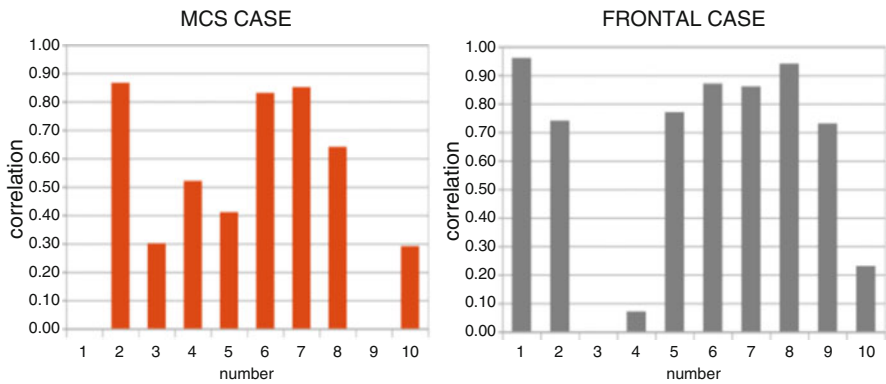
Fig. 4.8 Correlation coefficients between IWV from GNSS and WRF for (**a**) MSC and (**b**) frontal cases
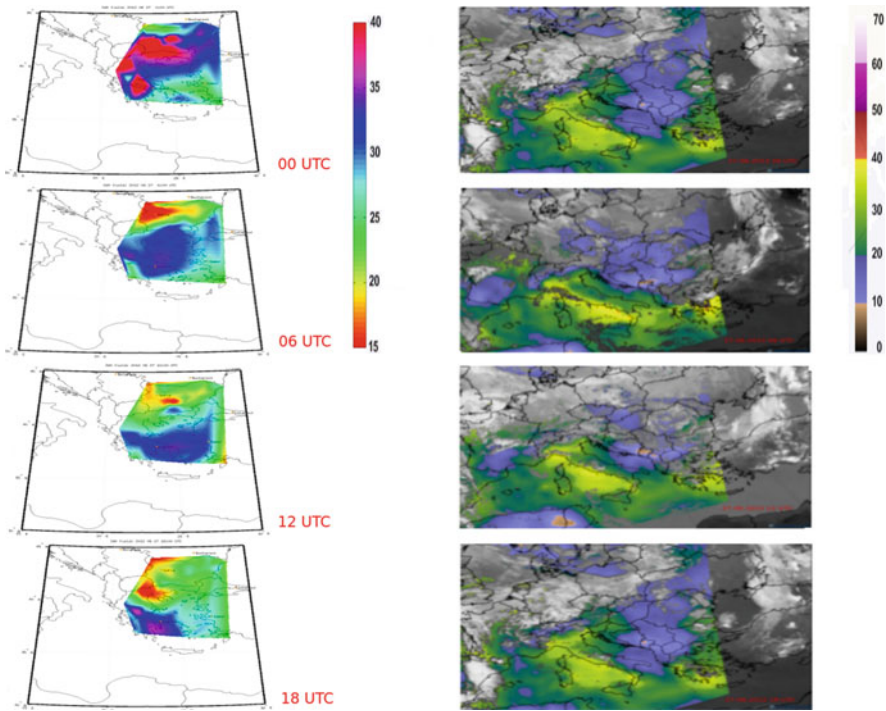

Fig. 4.9 2D maps of the GNSS IWV on 27 June at: (**a**) 00:00 UTC, (**c**) 06:00 UTC, (**e**) 12:00 UTC and (**g**) 18:00 UTC. 2D maps of the Meteosat-IWV on 27 June at: (**b**) 00:00 UTC, (**d**) 06:00 UTC, (**f**) 12:00 UTC and (**h**) 18:00 UTC. Note the difference in the colour map

of the model, (2) better model performance for frontal precipitation cases compared to the mesoscale convective systems and (3) potential for model improvement by assimilation of GNSS IWV. The work will continue by developing a pilot transnational severe weather service exploiting GNSS tropospheric products in collaboration with the colleagues from Cyprus and Greece.

4.2.3   Case Study of Foehn in Sofia with GNSS Tropospheric Products

K. Stoev
Sofia University "St. Kliment Ohridski", Sofia, Bulgaria
e-mail: krasi@phys.uni-sofia.bg

G. Guerova
Physics Faculty, Department of Meteorology and Geophysics, Sofia University "St. Kliment Ohridski", Sofia, Bulgaria
e-mail: guerova@phys.uni-sofia.bg

Foehn is an extreme weather event by wind speed and its accurate prediction is still a challenge in operational forecasting. The aim of this study is to use the GNSS derived water vapour to study the Foehn onset in Sofia valley.

Foehn is a warm and dry wind that blows on the downwind side of a mountain and due to its high wind speed and pulsating nature, it is also an extreme weather event impacting aviation, construction, agriculture and spread of fires. The Foehn in Sofia occurs usually during a south or southwest airflow. Passing over the Vitosha mountain the air descends to Sofia valley and adiabatically warms and dries. A cloud-wall forms on the upward side of the Vitosha mountain (blue shading in Fig. 4.10a) and an Altocumulus lenticularis cloud is observed from Sofia (grey shading in Fig. 4.10a). In this work we derive water vapour from IGS station in Sofia (SOFI, black pointer in Fig. 4.10a). Following Stoycheva et al. (2017) we compute Equivalent Potential Temperature (EPT) and Sofia Stability Index (SSI) using surface temperature observations from synoptic station in Sofia (600 m asl., blue pointer in Fig. 4.10a) and Cherni vrah (2290 m asl. Not shown). The Foehn in Sofia is related to the development and the trajectory of cyclonic vortices. In Fig. 4.10b are illustrated the cyclone tracks for four case studies.

Stoev and Guerova (2017) study Foehn in Sofia for the 40-year period (1975–2014) and report 280 days, summarized in 201 synoptic situations. The annual average number of the days with Foehn is 7. However, the number of days was found to be higher for the 1975–1990 period compared to 1990–2014. As seen from Fig. 4.11 this is also reflected in the number of days with wind speed classified according to the severe weather criteria of Meteoalarm. Namely, for the 1975–1990 period 26 Foehn days are with the wind speed below 14 m/s (green bars in Fig. 4.11), 69 days are with wind speed from 14 to 19 m/s (yellow bars in Fig. 4.11), 40 days are
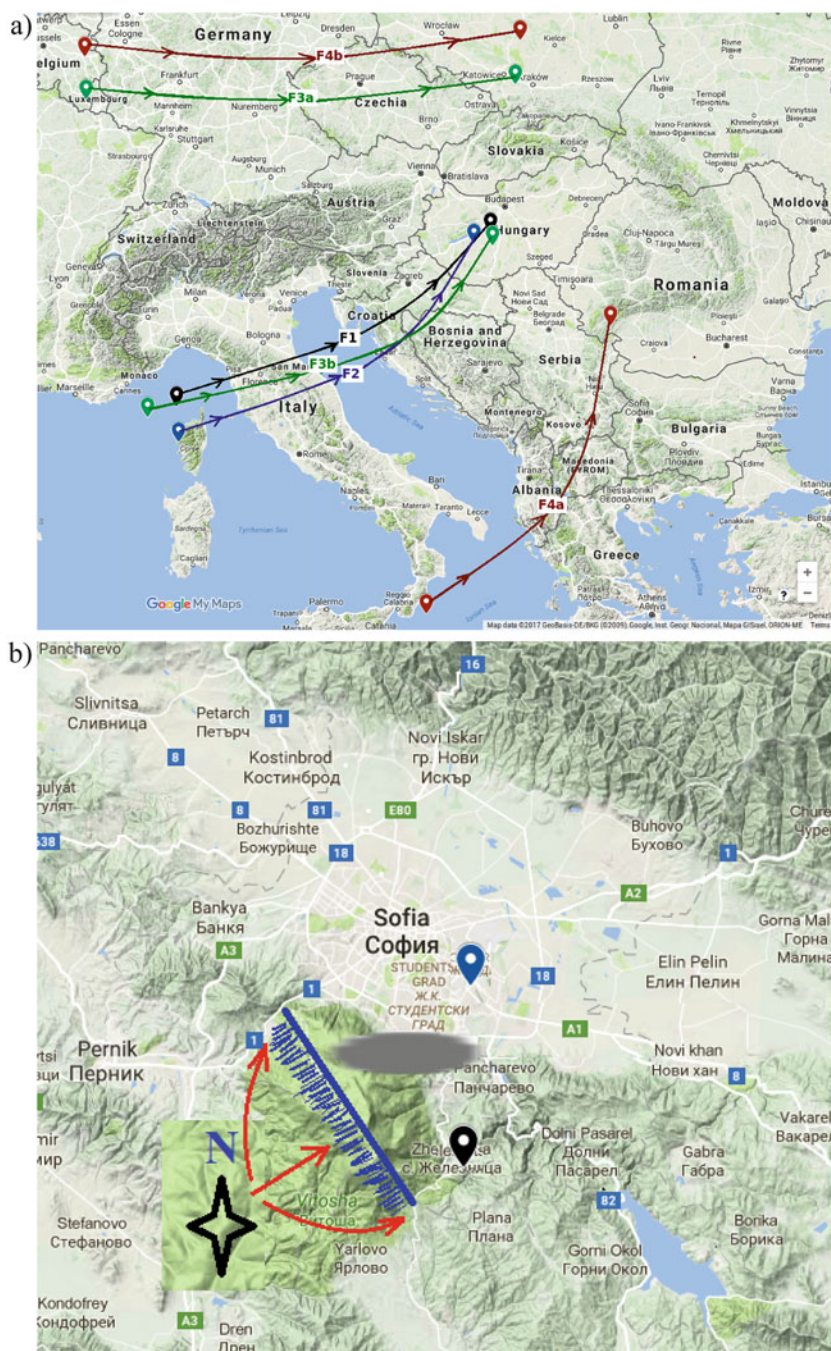
Fig. 4.10 (**a**) Map of Sofia valley and Vitosha mountain with GNSS station SOFI (black pointer) and Sofia synoptic station (blue pointer). The shaded blue area is the location of the cloud wall. (**b**) Cyclone tracks: (1) 24–26 March 2004 (F1 blue line), (2) 26–28 December 2004 (F2 black line), (3) 21–25 March 2008 (F3 green line) and (4) 3–7 December 2008 (F4 red line)
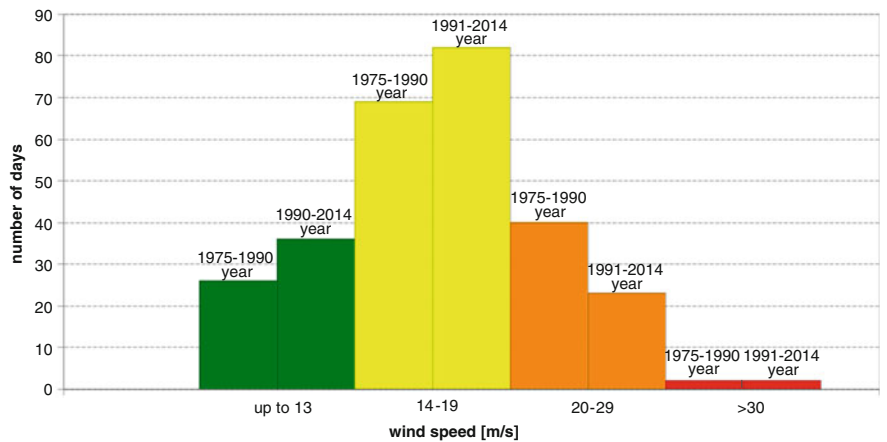
Fig. 4.11 Number of days with Foehn in Sofia for the 1975–1990 (left bars) and 1990–2014 (right bars). The colour code is following Meteoalarm severe weather criteria i.e. "green" for wind speed below 14 m/s, "yellow" for wind speed 14–19 m/s, "orange" for wind speed 20–29 m/s and "red" for wind speed higher than 30 m/s
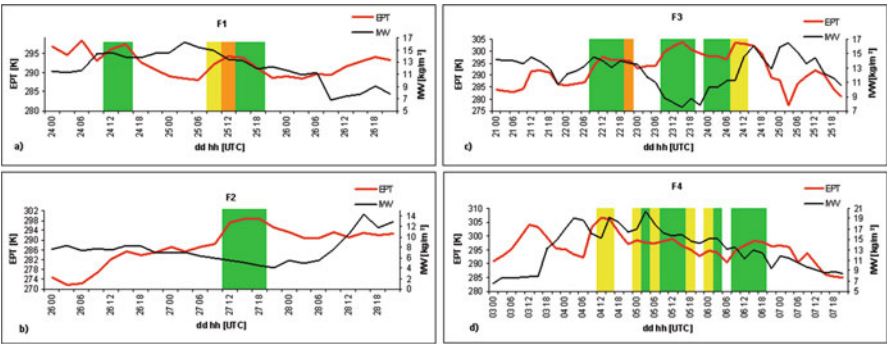

Fig. 4.12 EPT (red line) and IWV (black line), bars mark the foehn periods and bar colour corresponds to the Meteoalarm code for: (**a**) F1, (**b**) F2, (**c**) F3 and (**d**) F4

with wind speed 20–29 m/s (orange bars in Fig. 4.11). Compared to 1975–1990 for the 1990–2014 period the number of days with wind speed below 14 m/s and 14–19 m/s is higher but the lower number of days is recorded with wind speed 20–29 m/s.

Based on GNSS data availability four Foehn cases in 2004 and 2008 are investigated in this work namely: (1) *24–26 March 2004 (F1), (2) 26–28 December 2004 (F2), (3) 21–25 March 2008 (F3) and (4) 3–7 December 2008 (F4).* As seen in Fig. 4.12a two Foehn events are registered on 24 (12:00–18:00 UTC) and 25 March 2004 (9:00–21:00 UTC). Both of them start with EPT increase of 3.2 K/3 h and 4 K/

3 h correspondingly (Fig. 4.12a). The IWV decrease is registered during the foehn but no marked changes are observed before the Foehn start (Fig. 4.12a). The SSI has sharp decrease from 0.59 at 9:00 UTC to 0.29 at 12:00 UTC on 24 March (Fig. 4.12a). The Foehn is observed for a 9-hour period (12:00–21:00 UTC) on 27 December 2004. The EPT increased from 288.3 K at 9:00 UTC to 297.3 K at 12:00 UTC (Fig. 4.12b) and SSI decreased from 0.85 to 0.65 (Fig. 4.13b). IWV decreases linearly between 3:00 and 21:00 UTC on 27 December.

Foehn outbreaks with different duration are registered on 22, 23 and 24 March 2008. Marked increase of EPT from 287 to 294 K and from 293.9 to 299.8 K is seen between 6:00 and 9:00 UTC on both 22 and 23 March (Fig. 4.12c), correspondingly. It is to be noted while on 24 the EPT is constant. On 23 March, IWV starts to decrease from 13.5 kg/m^2 at 0:00 UTC to 8.8 kg/m^2 at 9:00 UTC (Fig. 4.12c). SSI drops from 0.61 to 0.36 between 6:00 and 9:00 UTC on 22 March (Fig. 4.13c). Foehn wind with different duration is registered on 4, 5 and 6 December 2008. As seen from Fig. 4.12d the EPT increased by: (a) 3.3 K/3 h (303–306.3 K), (b) 1.3 K/3 h (297.2–298.5 K), (c) 1.7 K/3 h (293–294.7 K) and (d) 4.5 K/3 h (290.2–294.5 K). The SSI decreased by: (a) 0.19 (0.79–0.6) 9:00 to 12:00 UTC on 4 December, (b) 0.4 (0.7–0.3) 21:00 to 0:00 UTC on 4–5 December, (c) 0.2 (0.5–0.3) 21:00 to 0:00 UTC on 5–6 December and (d) 0.2 (0.6–0.4) 6:00 to 9:00 UTC 6 December (Fig. 4.13d). On 5 December, IWV has steady decrease from 20.4 kg/m^2 at 3:00 UTC to 14.3 kg/m^2 at 21:00 UTC.

It can be concluded that the start of Foehn in Sofia is associated with sharp increase of equivalent potential temperature and drop of the Sofia Stability Index. However, the water vapour at SOFI station does not reflect the air mass change namely decrease with Foehn start. The likely reason is the SOFI station location, which is on the side of the Vitosha mountain. It is to be noted that the Foehn is very
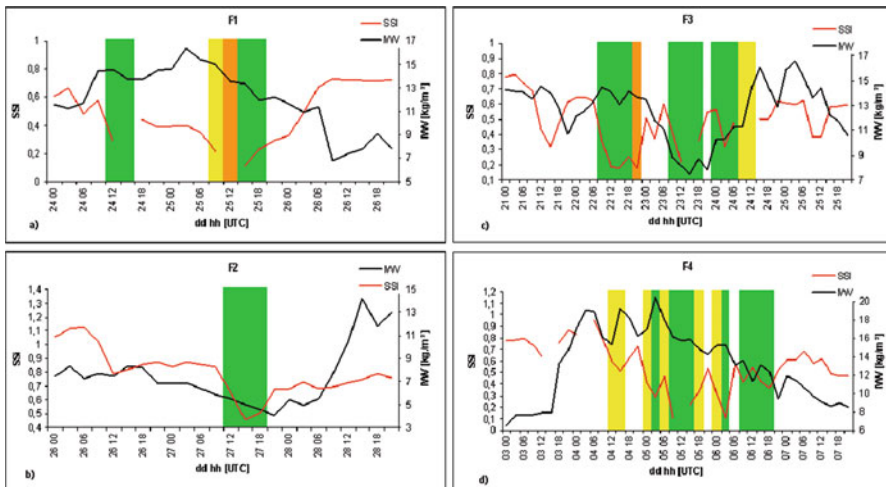

Fig. 4.13 SSI (red line) and IWV (black line) bars mark the foehn periods and bar colour corresponds to the Meteoalarm code for: (**a**) F1, (**b**) F2, (**c**) F3 and (**d**) F4

local phenomenon thus the station position plays a critical role. The work will continue by conducting case studies using GNSS station located in Sofia valley as a part of a pilot transnational severe weather service exploiting GNSS tropospheric products for the Balkan-Mediterranean region.

4.2.4   A GNSS-Based Nowcasting Toolbox for Severe Weather in Belgium

E. Pottiaux
Royal Observatory of Belgium, Brussels, Belgium
e-mail: eric.pottiaux@oma.be

C. Bruyninx
Royal Observatory of Belgium, Brussels, Belgium
e-mail: carine.bruyninx@oma.be

J. Berckmans
Royal Meteorological Institute of Belgium, Brussels, Belgium
e-mail: julieb@meteo.be

S. de Haan
Royal Netherlands Meteorological Institute, De Bilt, The Netherlands
e-mail: siebren.de.haan@knmi.nl

At the beginning of COST Action GNSS4SWEC, a workshop dedicated to review the state-of-the-art was organised in Munich, Germany. In that context, the Royal Observatory of Belgium (ROB) decided to review potential methods and products to develop a comprehensive prototype toolbox for non-numerical nowcasting that can be used to study severe weather cases, with a focus over Belgium and the BENE-LUX. This toolbox was then used on a real severe weather case study to evaluate its potential and performances, draw a non-exhaustive inventory of problems encountered and open questions related to non-numerical GNSS-nowcasting, fostering discussions within WG2 and new developments in the field.

The Case Study

To develop and assess our GNSS nowcasting toolbox, we chose to focus on a severe weather case that happened in a nowcasting domain (Lon: E 1°–E 7.5°, Lat: N 48.5°–N 53.5°) similar to the one used by the INCA-BE nowcasting tool and the operational NWP ALARO 4 km resolution model operated at Royal Meteorological Institute (RMI) of Belgium. This case happened at the end of the summer 2012 (16–26 September 2012), with a passage of a cold front with a warm front ahead on 23–25 September 2012. The synoptic situation is shown in Fig. 4.14. These fronts came from France and moved in the northeast direction, crossing Belgium and evacuating by the Netherlands. The system turned into the formation of an occluded front, which curved around the depression (i.e. back-bent occlusion) located south of
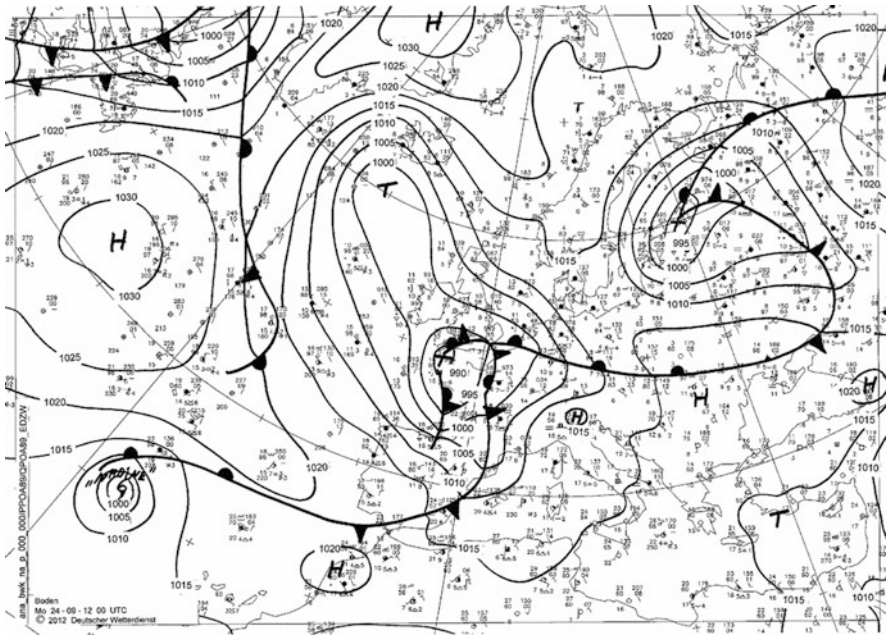
Fig. 4.14 Synoptic situation 24th Sept 2012 at 12:00 UTC. (Courtesy of DWD)
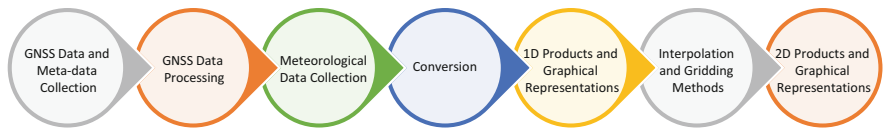
Fig. 4.15 Schematic structure of the toolbox in modules

U.K. During the night of the 23–24 September 2012, the weather system produced deep convective cells bringing heavy precipitation and severe wind in Belgium.

The Toolbox

The comprehensive toolbox developed includes several modules (Fig. 4.15) that relate to the data collection, data processing, and graphical representation.

GNSS Data Collection and Processing

To feed the toolbox with tropospheric products, the historical raw daily observations from 331 GNSS stations were collected from the EPN (EUREF Permanent Network, http://epncb.oma.be) and IGS (International GNSS Service, http://igscb.jpl.nasa.gov) networks, and completed with observations from the national densification networks in Belgium, France, Netherlands, and UK (Fig. 4.16). These historical daily observations have been analysed using the Bernese GNSS software (Dach et al. 2015) with the Precise Point Positioning (PPP) method (in post-processing) to

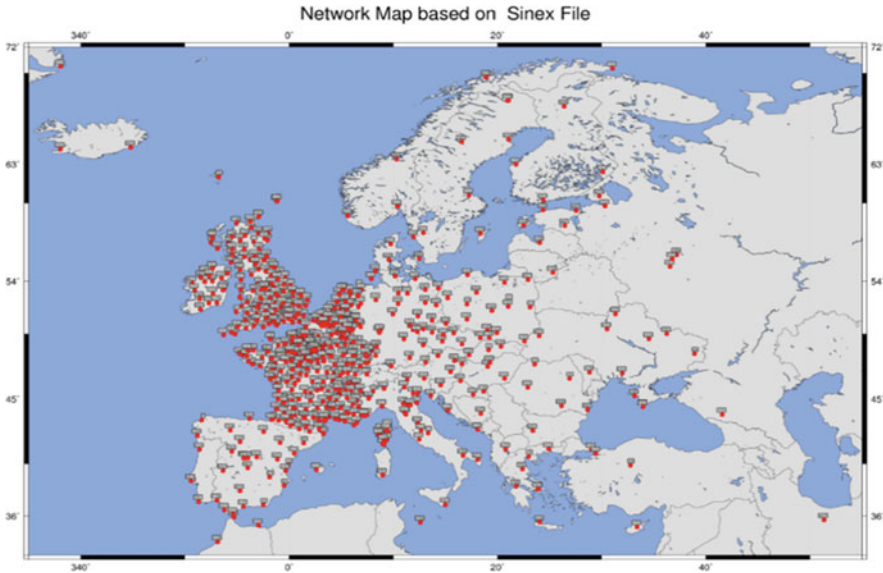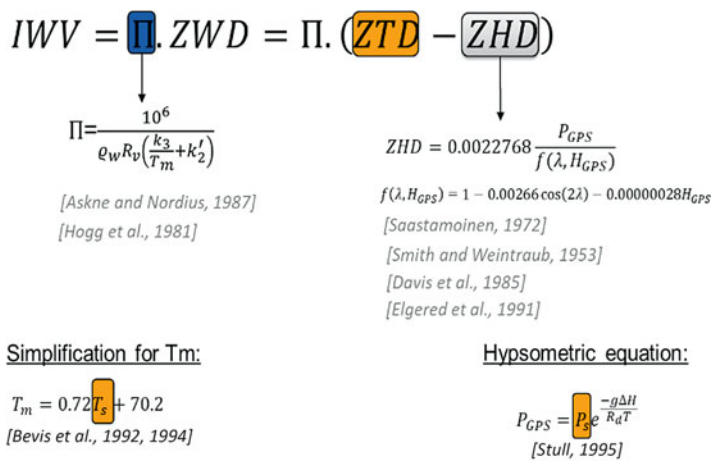**Fig. 4.16** Network of GNSS Stations processed during the case study

estimate tropospheric parameters with a time resolution of 5 min. The tropospheric parameters include Zenith tropospheric Total Delays (ZTDs) and tropospheric horizontal gradients (GRDs). Although not yet considered in the present study, ZTDs and GRDs can be used to reconstruct the slant tropospheric delays, and their potential for non-numerical nowcasting will be investigated in the future.

Meteorological Data Collection and IWV Conversion

The estimated ZTD were then converted into Integrated Water Vapour (IWV). For this, we chose a quite conservative and well-established approach found in the literature (Rocken et al. 1995; Wang et al. 2005, 2007; Heise et al. 2009; Vey et al. 2009; Ning et al. 2013; van Malderen et al. 2014) (Fig. 4.18). The conversion requires surface pressure and surface temperature data at the GNSS station location. Therefore, we collected meteorological data from 135 meteorological sensors (red dots in Fig. 4.17). These sensors belong to the RMI (Belgium), KNMI (The Netherlands), and the Integrated Surface Data (ISD, NOAA) observation networks. To obtain the surface pressure and temperature at the GNSS station, we used the nearest meteorological sensor (i.e. no time nor spatial interpolation was carried out), with a max distance of 50 km, a max altitude difference of 500 m, and a max time differences between meteorological and ZTDs observation epochs of 5 min to ensure the quality of the conversion. Even if more sophisticated approaches can be applied (e.g. a weighted mean interpolation in space and a temporal interpolation), the current simple approach gave satisfactory results for our study.

Fig. 4.17 Location of the GNSS stations (blue dots) and meteorological sensors (red dots) located in the nowcasting domain considered (orange dashed line)

Conversion Error and User Product Requirement

Using the method presented in Fig. 4.18, the nearest meteorological sensor, and the findings presented in (Bevis et al. 1994; Ning et al. 2013), we estimated that the total uncertainty of our IWVs is in the 0.75–1.03 mm range. This means that the requirement for non-numerical nowcasting (Table 4.2) are achieved.

Basic Graphical Representation

Most graphical modules of the toolbox relies on the Generic Mapping Tools (GMT, http://gmt.soest.hawaii.edu/home). They enable the representation of the products (e.g. the IWV) both in time and in space. It includes time series (Fig. 4.20) and maps (Fig. 4.19) representations. These graphical outputs can then directly be published on a web user-interface to enable studying and interpreting the weather conditions.

Interpolation Methods for Reconstructing Grids

In addition to the point representation in space shown in Fig. 4.19, we wanted the toolbox to be able to fully represent the IWV field over the complete nowcasting

$$IWV = \Pi \cdot ZWD = \Pi \cdot (ZTD - ZHD)$$

$$\Pi = \frac{10^6}{\varrho_w R_v \left(\frac{k_3}{T_m} + k_2'\right)}$$

[Askne and Nordius, 1987]

[Hogg et al., 1981]

$$ZHD = 0.0022768 \frac{P_{GPS}}{f(\lambda, H_{GPS})}$$

$$f(\lambda, H_{GPS}) = 1 - 0.00266 \cos(2\lambda) - 0.00000028 H_{GPS}$$

[Saastamoinen, 1972]

[Smith and Weintraub, 1953]

[Davis et al., 1985]

[Elgered et al., 1991]

__Simplification for Tm:__

$$T_m = 0.72 T_s + 70.2$$

[Bevis et al., 1992, 1994]

__Hypsometric equation:__

$$P_{GPS} = P_s e^{\frac{-g\Delta H}{R_d T}}$$

[Stull, 1995]

Fig. 4.18 Scheme of the method used to convert ZTDs to IWVs

Table 4.2 Requirement imposed on IWV observations for non-numerical nowcasting applications as stated in the E-GVAP Product Requirement Document [E-GVAP PDR]

	Threshold	Breakthrough	Goal
Accuracy	5 kg/m^2	2 kg/m^2	1 kg/m^2
Timeliness	30 min	10 min	5 min

domain. Therefore, four interpolation methods have been implemented, and their performances intercompared. These methods are the optimal triangulation (Watson 1982), the Nearest Neighbour, the Continuous Curvature Spline in Tension (Smith and Wessel 1990), and the Ordinary Krigging (Matheron 1962, 1963a, b) methods. An example of this comparison is given in Fig. 4.21. The optimal triangulation and nearest neighbour methods gave unsatisfactory results (with sometimes unrealistic IWV local field, incomplete domain fill, artefacts...) while the continuous curvature spline in tension and ordinary Krigging methods gave a more realistic IWV field representation over the full nowcasting domain. The two latest methods are also the two methods that match the more closely together. The Krigging method has the advantage to be capable to take into account the uncertainties in the input data, and to enable the estimation of the variance of the estimated grid, i.e. the uncertainty of our IWV field over the whole domain. For example, in the case presented in Fig. 4.21 the error variance of the estimated IWV field remained below 1.2 mm (Fig. 4.22, right), satisfying the nowcasting requirements (Table 4.2). We thus opted for the Ordinary Krigging method to reconstruct maps with a time resolution of 5 min and a spatial resolution of 0.05° lon. × 0.05° lat. The toolbox also allows applying a mask over some regions like the Channel and U.K. as shown in the figures below.
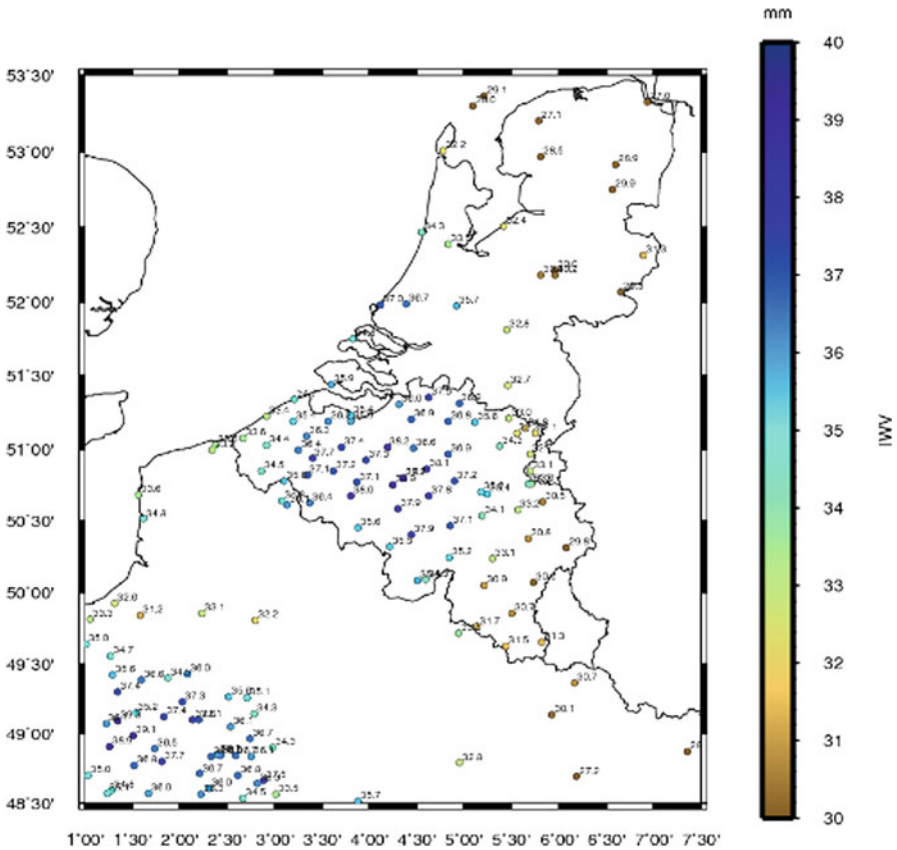
Fig. 4.19 Spatial representation of the IWV at each GNSS station at epoch 23 Sep. 2012 23:00 UTC

Exploiting the Horizontal Gradients to Access the Horizontal Inhomogeneity

During the GNSS data processing, N-S and E-W tropospheric horizontal gradients (GRDs) were estimated simultaneously to the ZTDs with a time resolution of 5 min. The GRD estimation follows the methodology proposed in (Chen and Herring 1997), and represents the first-order heterogeneities in the tropospheric delay (mainly due to water vapour but not only). These GRDs can be used to study the location of water vapour inhomogeneities in the atmosphere. The toolbox allows representing them in the form of time series (Fig. 4.23) or superimposed them over 2D grid maps (e.g. IWV maps, Fig. 4.24).

During our analysis we noticed at several occasions that horizontal gradients at nearby or collocated GNSS stations showed sometimes a very good agreement but sometimes emphasized very different directions (e.g. in Fig. 4.25). Therefore, we currently recommend a careful usage of horizontal gradients until further investigations on the validation and representativeness of the GRDs are carried out. Such investigations can e.g. be done based on long-term GRD observations at collocated

23/09/2012 23:00 UTC
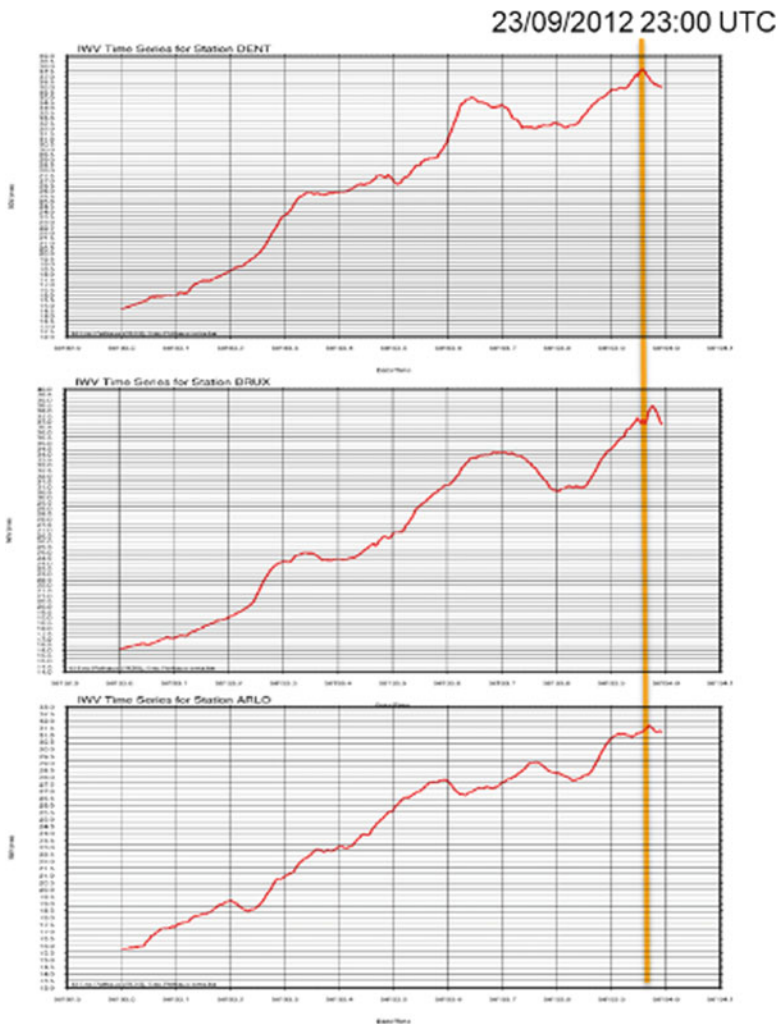
Fig. 4.20 Time series of the IWV at three Belgian stations (top: Dentergem, middle: Brussels, bottom: Arlon)

GNSS stations, and cross validated with external source of information whenever possible (e.g. output of NWP models that doesn't assimilate GNSS products). In addition, the impact of the antenna calibration model on the estimation of the horizontal gradients should be investigated (e.g. type mean versus individual calibration, and antenna misalignment).

Computing Reconstructed Grid Derivatives
Once the 2D grid map has been reconstructed based on the Ordinary Krigging interpolation method, the 2D map of partial derivatives in the N-S and E-W
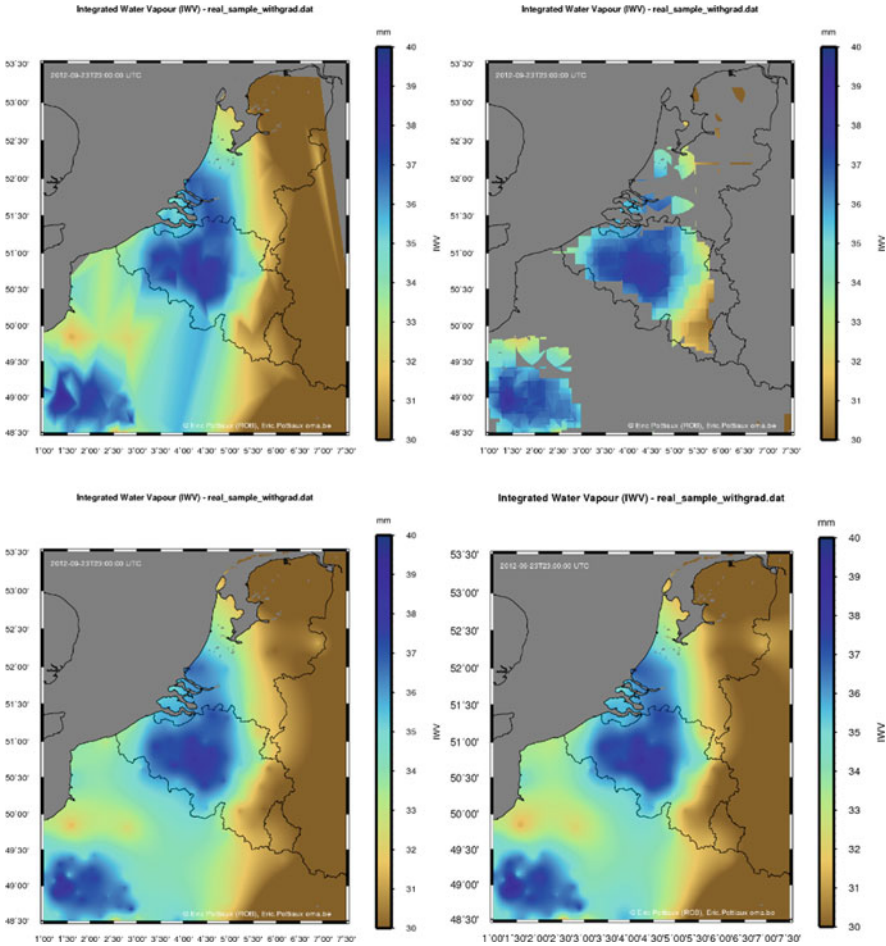
Fig. 4.21 IWV maps derived from the four interpolation methods implemented (Top left: optimal triangulation, top right: nearest neighbour, bottom left: continuous curvature spline in tension, and bottom right: ordinary krigging) on 23rd Sep. 2012 at 23:00 UTC. Grids are clipped to remove the field over the Channel and U.K

directions can be computed from the original grid, e.g. for the IWG grid. These partial derivative maps can then be used to study the heterogeneities in the IWV field and might also be used to intercompare with the horizontal gradient components computed during the GNSS processing. Figure 4.26 show an example of the 2D map of the partial derivative norm at each IWV grid cell projected in the N-S (left plot) and E-W (right plot) directions with superimposed the GRDs estimated from the GNSS processing (red vectors). Similar plots can be constructed for the phase (direction) of the partial derivatives of the IWV grid.
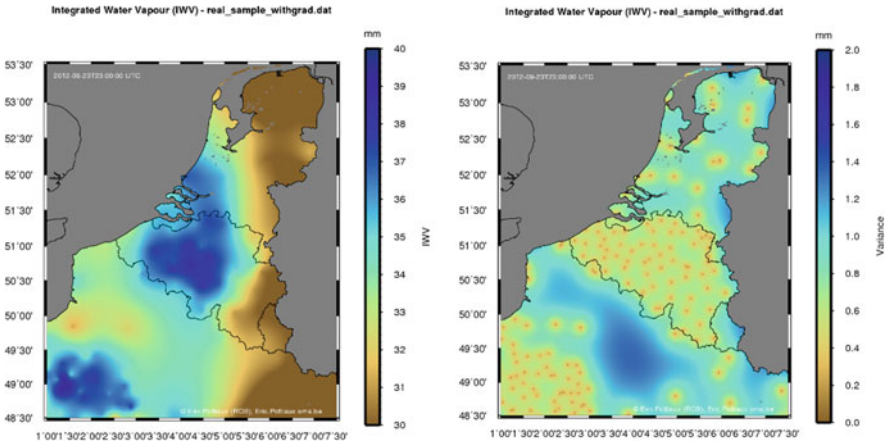
Fig. 4.22 Estimated IWV map based on the ordinary Krigging method (left) and its associated error variance (right)
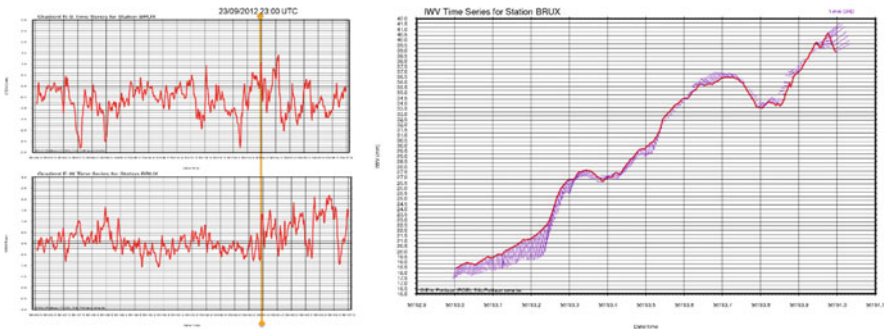
Fig. 4.23 (Left) Time series of the N-S (top) and E-W (bottom) GRDs estimated at the station BRUX in Brussels, Belgium. (Right) Time series of the ZTDs (in red) at the same station BRUX. Purple vectors superimpose the horizontal gradient attached at the ZTD point. The length of the vector represents the amplitude of the GRD and the direction of the vector gives the direction of the gradient in the horizontal plane (North is pointing to the top of the figure, East at the right...)

Extracting Tracks Through the Reconstructed Grid

Another important capability of the toolbox is to enable the extraction of specific profile along a track in the interpolated grid field, as specified by its origin and destination coordinates. An example is given in Fig. 4.27 with an IWV grid map. Extracting track profile enable e.g. to study the IWV distribution along a path crossing a specific region. Such specific region can e.g. be a deep convection cell causing severe rain as illustrated with the radar image in Fig. 4.27. Similarly as for IWV, track profiles can be extracted from other 2D grid field representation (e.g. partial derivative grids) reconstructed by the toolbox, and presented later (e.g. partial derivatives) (Fig. 4.28).
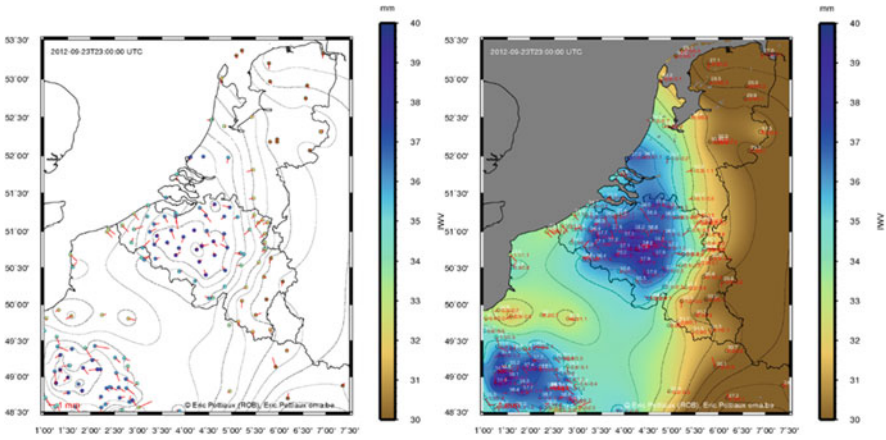
Fig. 4.24 Red vectors attached at the GNSS station location represent the tropospheric GRDs. The length of the vector matches the amplitude of the GRDs while the direction of the vector matches the orientation of the horizontal gradients
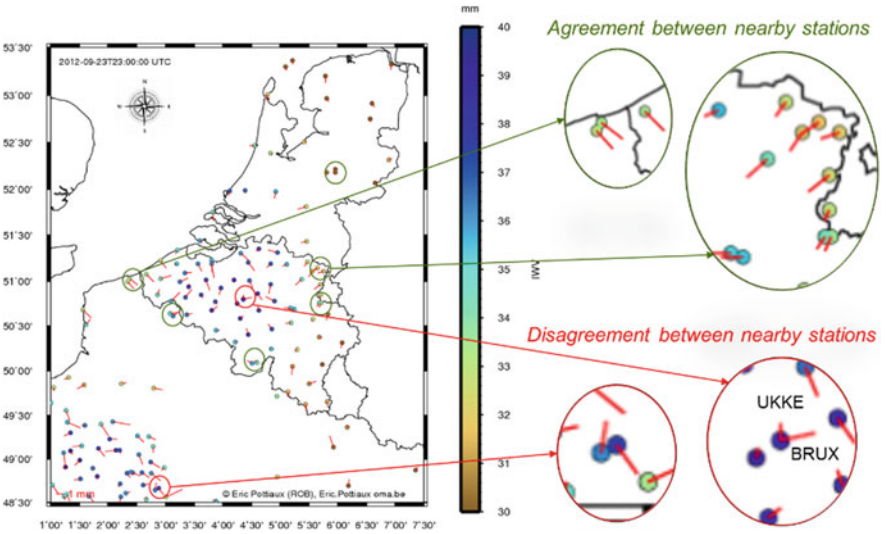

Fig. 4.25 Horizontal gradients superimposed on top of a point-wise ZTD map representation showing that GRDs sometimes agree very well but sometimes differs significantly in direction at nearby and collocated GNSS stations

Fluxes – Rate of Change – Post-fit Residuals Analysis

The developed toolbox also computes the fluxes or rate of changes of the IWV, and of the GRDs to detect sudden changes in water vapour distribution that might be associated with severe weather events like a deep convective system. An example is given in Fig. 4.30 showing the time series of the rate of change of the IWV (top), N-S
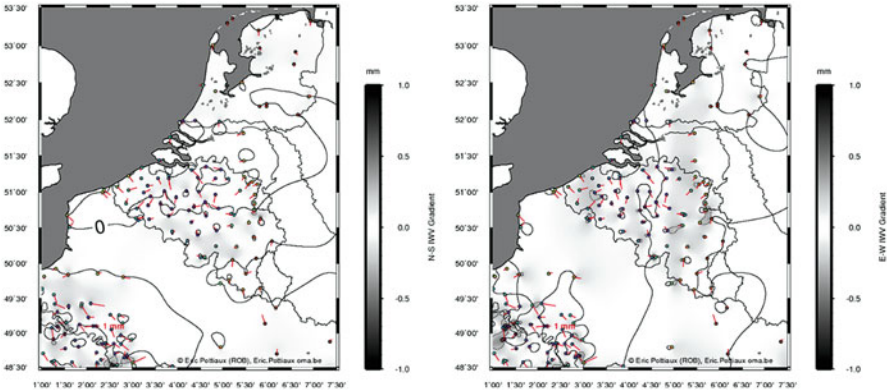
Fig. 4.26 Amplitude of the partial derivatives of the ZTD grid in the N-S (left) and E-W (right) direction. Superimposed (in red) the vector of the horizontal gradient estimated during the GNSS processing
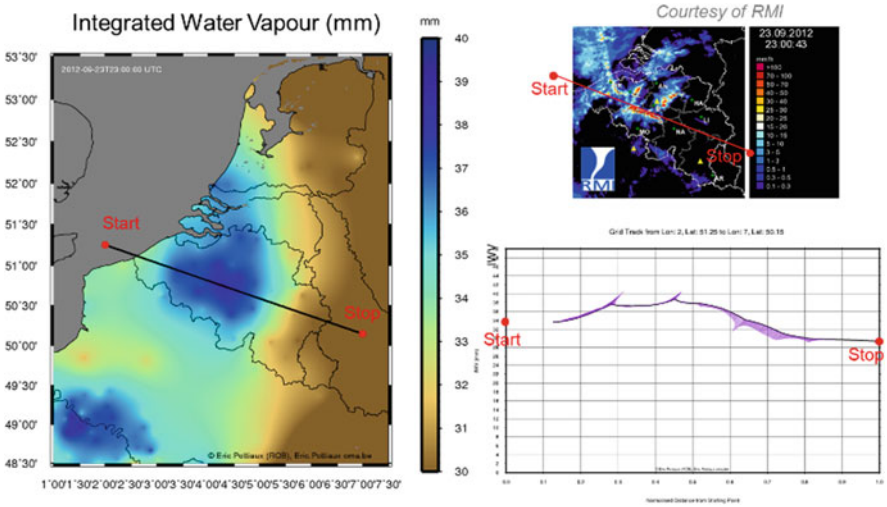
Fig. 4.27 (Left) IWV map reconstructed with Krigging interpolation on 23 Sep. 2012 23:00 UTC, and the track path superposed. (Top right) the corresponding radar image with the same track path aligned to a rain cell. (Bottom right) the IWV profile along the track

(middle), and E-W (bottom) gradients at Brussels, Belgium. A clear and sudden signature can be noticed at the moment when a deep convective system was passing over Brussels (orange vertical line). Once the fluxes/rate of change of these quantities are computed, the toolbox is also capable to reconstruct the 2D field of these rate of change (based on the interpolation methods presented above) to enable the study of their spatial and spatio-temporal (e.g. film) behaviours (Fig. 4.30). Finally, this information can also be combined with the analysis of the ionosphere-free carrier-
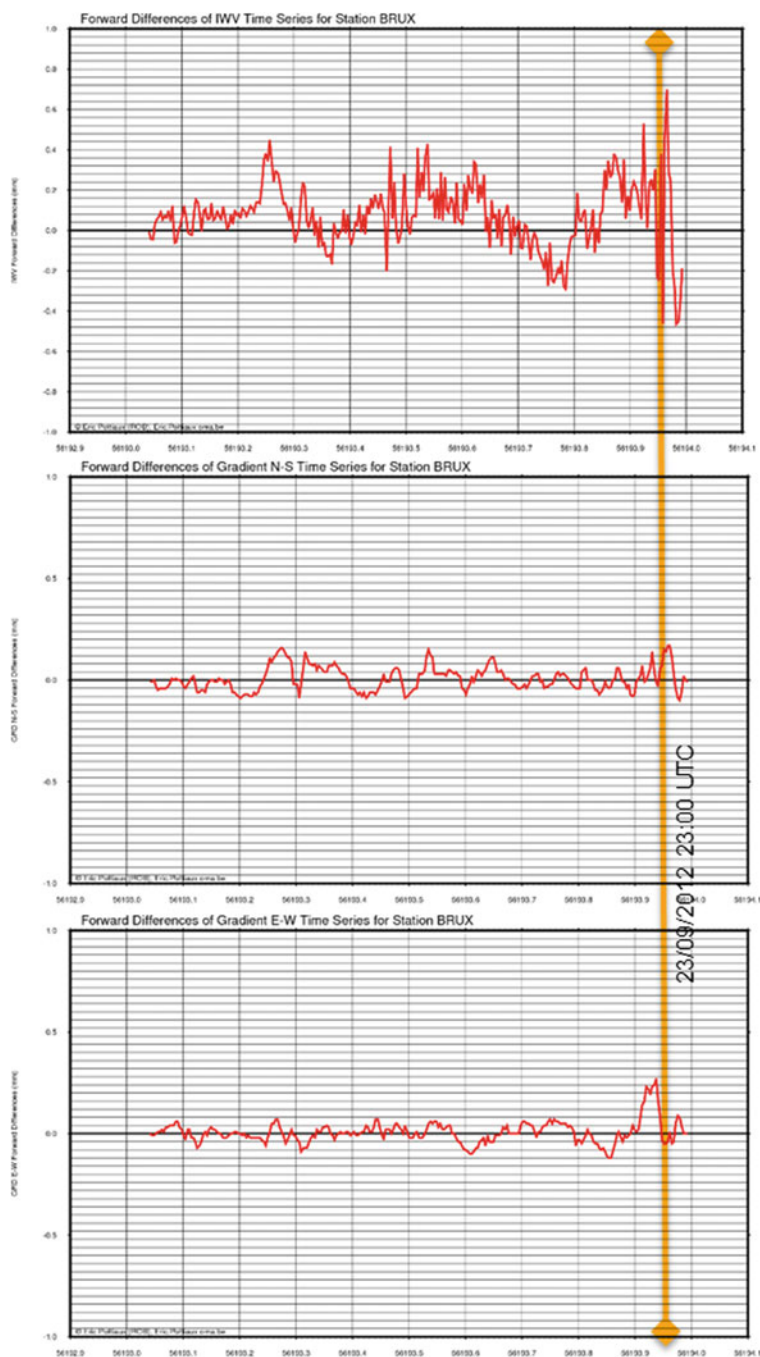
Fig. 4.28 Time series of the rate of change of the ZTD (top), N-S (middle) and E-W (bottom) GRD at Brussels, Belgium
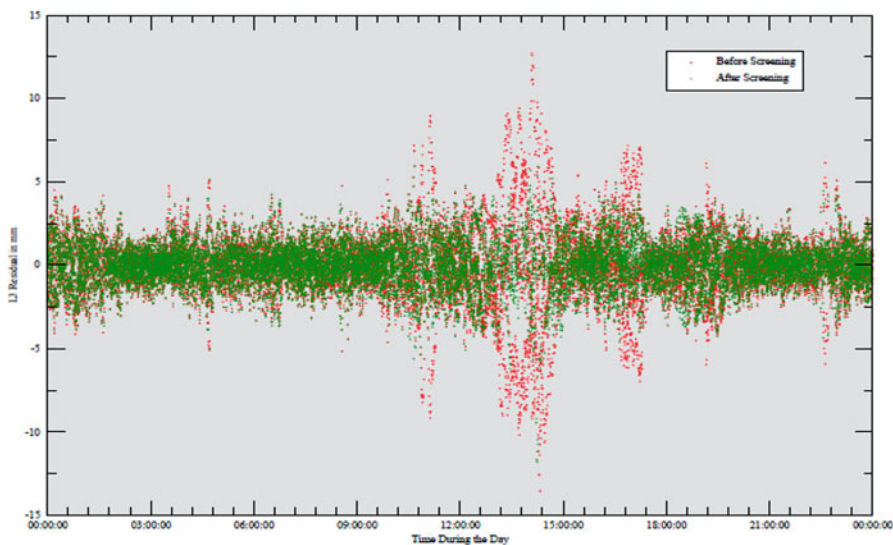
Fig. 4.29 Ionosphere-free carrier-phase double-difference post-fit residuals before (red dots) and after (green dots) data cleaning for the baseline Dentergem – Waremme, Belgium, during 29 June 2005. The passage of a deep convective system leading to a hailstorm

phase double-difference post-fit residuals before and after data cleaning as shown in Fig. 4.29 [Pottiaux 2010]. Altogether, these fluxes/rate of change, and post-fit residuals quantities are very important quantities in the process of setting up automatic detection of severe events and alarms systems based on critical values (Fig. 4.30).

Conclusions and Open Questions

With the development of a prototype GNSS-based nowcasting toolbox, the Royal Observatory of Belgium (ROB) aimed to demonstrate the feasibility, and to foster GNSS-based non-numerical nowcasting in Belgium and the BENELUX. The current toolbox includes numerous 1D and 2D representation of various tropospheric quantities (ZTD, IWV, GRD, fluxes/rate of change...) with sufficient precision to allow studying the spatio-temporal evolution of water vapour for nowcasting. 2D representation can be stacked over time to create movies representing the time evolution. The toolbox also enables the operation of automatic detection of severe events, and to trigger alarms (e.g. based on the rate of change and post-fit residuals), albeit the necessary critical values and pattern recognition should be further studied.

During the developments, a list of further investigations was established, and includes e.g. assessing the horizontal gradients and studying their representativeness in some cases, an automatic access to and an enhancing of the use of surface pressure and temperature data (e.g. interpolation method for the conversion or testing the use of the forecast fields from high-resolution NWP models), and accessing GNSS tropospheric products with a latency below 5 min to operate such toolbox in live conditions.
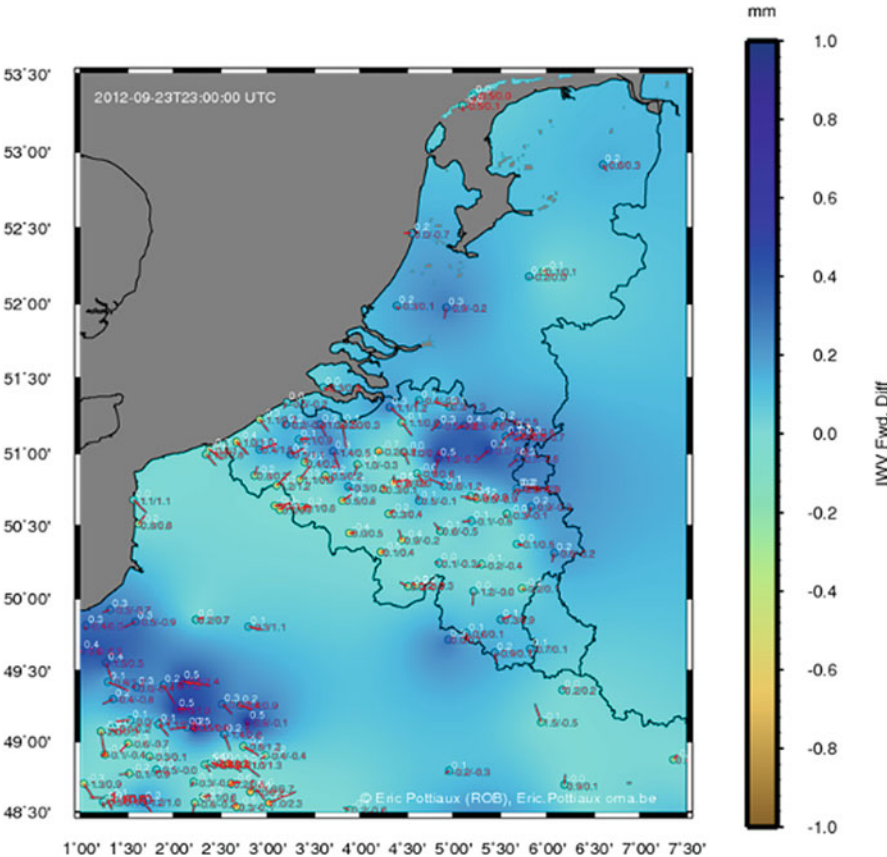
Fig. 4.30 2D field of the rate of change of the IWV in the nowcasting domain superimposed with the horizontal gradient information.

Operating live this toolbox requires indeed a real-time access and processing of the GNSS observations. Therefore, within the real-time demonstration campaign of the WG1, ROB collaborated with the GOP (Geodetic Observatory in Pecný) to use their GNut/Tefnut software, and to setup at ROB a prototype real-time processing of GNSS observations in this nowcasting domain, including the Belgian dense network. This activity was started during the context of a Short-Term Scientific Mission (STSM) of the Action, and enable to feed the toolbox with real-time ZTD, GRD and slant delays.

Until now, we operated the toolbox over a single case study to demonstrate its potential. Of course, the next natural step would be to operate it, and to test it over a wider variety of cases. For this, operating live the toolbox would be very beneficial. This would also enable to contribute updating and extending the requirements imposed for non-numerical nowcasting as found in the current version of the E-GVAP Product Requirement Document [E-GVAP PDR].

Finally, as shown with one example of radar images, this toolbox would highly benefit of a synergetic use with other meteorological observation sources such as radars, Meteosat, winds, lightning, SSMI... observations, as it was already demonstrated in the literature (Mazany et al. 2002; de Haan et al. 2004, 2009). However, one has to note that this synergetic use would probably better find its place directly within a nowcasting suite such as the INCA-BE rather than in a separate toolbox.

4.3 Numerical Nowcasting and NWP Data Assimilation

4.3.1 HARMONIE-AROME Group

M. Lindskog
Swedish Meteorological and Hydrological Institute, Norrkoping, Sweden
e-mail: magnus.lindskog@smhi.se

J. Sánchez-Arriola
AEMET, Santander, Spain
e-mail: jsancheza@aemet.es

The benefit of using GNSS ZTD in the state-of the art HARMONIE-AROME km scale data assimilation and forecasting system has been demonstrated (Sánchez-Arriola et al. 2016). A 3-dimensional variational data assimilation was applied and the importance of using an extensive observation handling was pointed out, and in particular the benefit of using an adaptive so called variational bias correction. For HARMONIE-AROME the sensitivity of the bias correction to adding additional refinements in the form of various additional predictors was small (Lindskog et al. 2017). On the other hand, results were found to be sensitive to the spatial density of the GNSS ZTD observations, due to the fact that a higher observation density does not necessarily imply better model skill, but no clear recommendation on optimal data density for a particular modelling system yet exist.

Since June 2016 Lantmäteriet (Swedish Mapping, Cadastre and Land Registration Authority) became NGAA, one of the analysis centres in E-GVAP and is in charge of the data processing for the GNSS stations in Sweden, Finland, Norway, Denmark and some IGS stations in order to provide near real-time (NRT) ZTDs. Currently NGAA has two NRT ZTD products (NGA1 and NGA2) produced. The NGA1 product is obtained from the BSW52 network solution while NGA2 is given by the GIPSY/OASIS II v.6.2 data processing using the Precise Point Positioning (PPP) strategy. We have validated the NGAA products by the ZTDs estimated by a post-processing using the IGS final satellite orbits and clock products. Two products give very similar results with a mean difference smaller than -0.5 mm and standard

deviations less than 5 mm with respect to the ZTDs from the post-processing. In addition, products of NGAA have also been compared and used within the state-of-the-art MetCoOp operational modelling system (Muller et al. 2017). The NGAA product has been shown to be beneficial to the forecast quality (Lindskog et al. 2017) and the NGAA product is now used operationally within the operational MetCoOp modelling system.

4.3.2 Assimilation of E-GVAP ZTD Data into the WRF Model

K. Eben · J. Resler · P. Krč
Institute of Computer Science of the Czech Academy of Sciences, Prague, Czech Republic
e-mail: eben@cs.cas.cz

We have performed several experiments, assimilating the ZTD from the E-GVAP database together with other data into the WRF model, using 3DVar assimilation package, WRFDA. In particular, we have investigated the synergy of the OPERA radar composite with E-GVAP data. We have tested different assimilation methods, among others the hybrid ensemble/3DVar method.

The OPERA radar composite provides a large source of European-wide data on radar reflectivity. E GVAP and OPERA bear different kind of information on water vapour in the atmosphere and both have a potential for data assimilation. Several simulations have been performed and analysis increments have been compared, using different background covariance models and analysis methods. Besides the standard 3DVar we used the ensemble/3DVAR hybrid method of Wang et al. (2008) with five control variables. This method combines the flow-dependent covariance derived from the ensemble with the climatologic (static) background covariance. The static part of the covariance was generated from historical data by the NMC method. The ensemble part was computed by means of downscaling the NCEP/GEFS ensemble using the WRF model. As expected, the hybrid method improves the estimate of the background covariance matrix. The NCEP/GEFS ensemble (20 members) seems to be suitable for use within the hybrid method. Figure 4.31 shows an example of a Pseudo single-observation test, where the pseudo observation is 1 cm above the model value of the ZTD.

For the benchmark test case (high precipitation episode in Bohemia in July 2013) we have performed several simulations of a forecast with the WRF model. We have compared water vapour increments when assimilating either E-GVAP ZTD or OPERA reflectivities. Water vapour increments from both radar and ZTD observations occur in higher model levels (model level 15 in Fig. 4.32 below) and are to some extent complementary. A typical pattern can be seen in Fig. 4.32.

Both ZTD and maximum reflectivity from OPERA have been assimilated, on the top of conventional observations. Starting from assimilated fields, a 24-hour
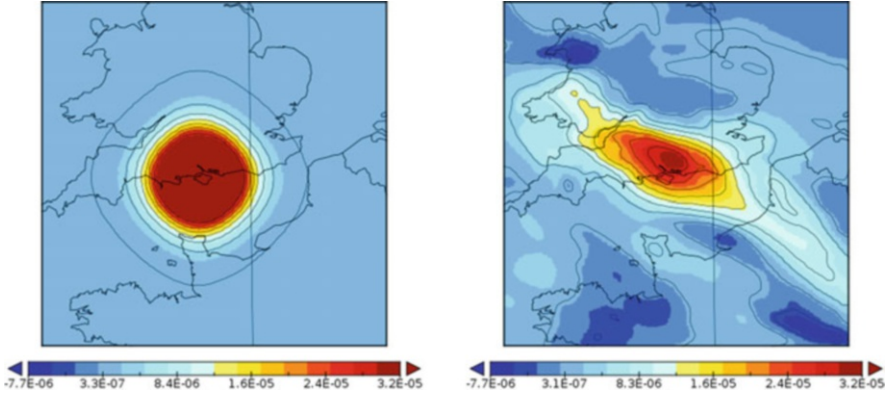
Fig. 4.31 Pseudo single-observation test. Left: analysis increment, static (isotropic) background covariance generated by the NMC method. Right: increment, hybrid covariance matrix with ensemble part derived from downscaled GEFS ensemble
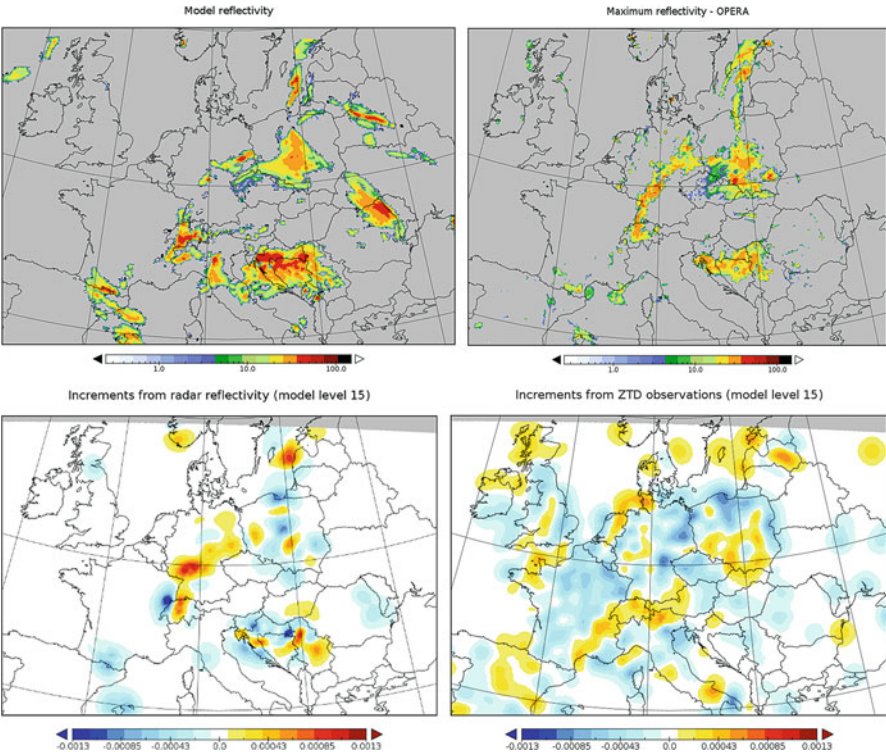

Fig. 4.32 A sample from an intensive rain episode (01 June 2013 03:00). Upper left: model maximum reflectivity, upper right: observed maximum reflectivity in OPERA composite. Lower left: Water vapour analysis increments from E-GVAP ZTD, lower right: analysis increments from OPERA reflectivity. There is no clear agreement between increments from ZTD and from reflectivity. The absence of ZTD increments in Serbia region is caused by the lack of measurements

accumulated precipitation has been forecast. The accordance of the forecast with observations is good. For 24-hour accumulated precipitation, however, only minor and non-systematic improvement over the operational forecast has been observed (Fig. 4.33).

The experiments confirm the widely accepted fact that GNSS observations represent a valuable source of data for assimilation. They provide an additional information on water vapour profile, which is complementary to radar reflectivities. The NCEP/GEFS ensemble seems to be promising in providing ensemble perturbations for the hybrid ensemble/3DVar method. The sensitivity of the forecast to background covariance is high and several settings of the methods need to be tuned before a stable forecast improvement may be expected.

4.3.3 Improvement of Forecast Skill of the GLAMEPS Model

L. De Cruz
Royal Meteorological Institute of Belgium, Brussels, Belgium
e-mail: lesley.decruz@meteo.be

E. Pottiaux
Royal Observatory of Belgium, Brussels, Belgium
e-mail: eric.pottiaux@oma.be

During the course of this COST Action, a Belgian nationally funded project was run at the Royal Meteorological Institute (RMI) of Belgium with the aim to improve the forecast skill of the probabilistic Grand Limited-Area Model Ensemble Prediction System (GLAMEPS) system (Smet et al. 2012; De Cruz and Duerinckx 2015). Key to the skill of the probabilistic forecast delivered by GLAMEPS is the accuracy of the constituent models of this ensemble. The progress in both data assimilation (DA) methods and novel observations have been indispensable in the increase in forecast skill of Numerical Weather Prediction (NWP) models in the past decades. As such, it is crucial that the current trend towards higher spatial resolutions in both deterministic and probabilistic models, such as GLAMEPS, is accompanied by a corresponding improvement in the model initialization. To this end, precipitation radar and GNSS tropospheric delay estimates (3D-var approach) data assimilation was implemented for the Belgian Local Area Model (LAM) ALARO.

ZTD Assimilation System
Where possible, the precipitation radar data assimilation was built upon the methods developed at Météo France for the assimilation of radar data using the Bayesian
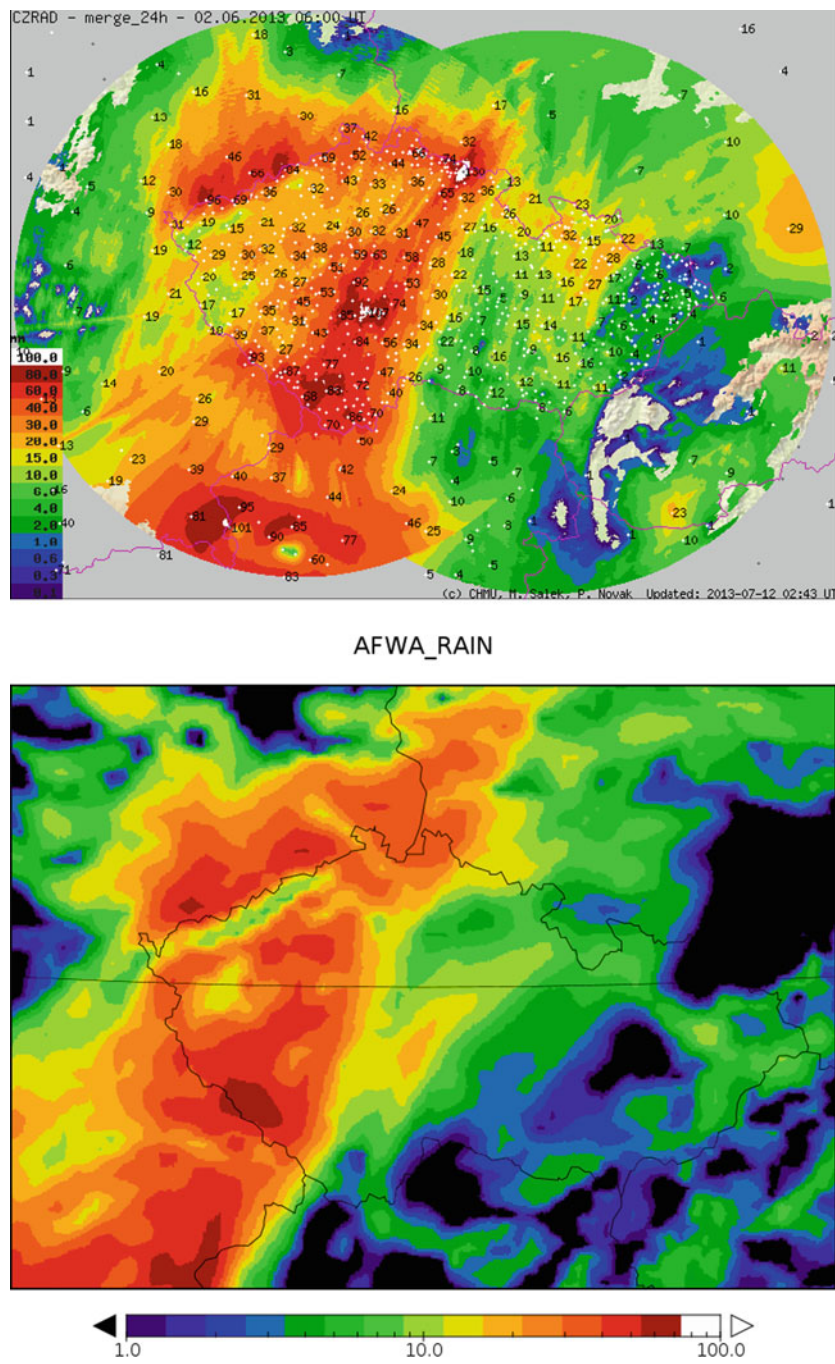
AFWA_RAIN

Fig. 4.33 Top: Estimated precipitation from radar and rain gauge sets (source: Czech Hydrometeorological institute). Bottom: WRF forecast of 24 h accumulated precipitation (1 June 2013 06:00–2 June 2013 06:00), starting from analysis with assimilated E GVAP ZTD and OPERA reflectivities. Time of analysis 01 June 2013 00:00

1D + 3DVar approach. This approach has been shown to significantly increase forecast skill in the first 12 h lead time (Caumont et al. 2010; Wattrelot et al. 2014). Then, the ZTD data assimilation system was developed based on the current 3D-Var system which was built for the assimilation of conventional data. The observation operator for the ZTD is calculated as the integral of the index of refractivity in the air column above the GNSS station location. This integral depends on the model pressure, temperature and partial pressure of water vapour. The GNSS ZTDs were processed and provided by the Royal Observatory of Belgium (ROB) (Pottiaux 2010; Bruyninx et al. 2012). It benefits from observations from the very dense network of GNSS tracking stations available in Belgium. In addition to radar and GNSS ZTDs, conventional ("SYNOP") observations such as weather station and sounding data were also assimilated.

Before assimilation of the ZTD data, a number of pre-processing steps were performed:

- Static bias correction, which is performed by calculating the differences between the simulated and observed ZTDs in a passive model run of 30 days (i.e., with assimilation of conventional data but not ZTDs). The static bias correction also takes into account the constant bias due to the fraction of the atmosphere above the highest model level.
- Based on the above error statistics, a white-list has been built for the GNSS stations.
- Spatial thinning was performed at the level of 10 km. Temporally, only the observations at assimilation time were retained: for example, in a 6 h update cycle, only the observations at 00, 06, 12, 18 h were retained.
- The hydrostatic correction, that accounts for the difference between the model altitude and the true altitude of the GNSS station, is accounted for in the observation operator.

The assimilation of ZTDs has a clear impact on moisture-related variables, as illustrated by the total precipitable water (TWP) in Fig. 4.34.

Results

The assimilation of ZTD data was shown to improve the representation of humidity in the low to middle troposphere (Yan et al. 2009), the prediction of precipitation patterns (Poli et al. 2007; Vedel et al. 2004), and cloud forecasts (Bennitt and Jupp 2012). In order to evaluate the impact of ZTDs assimilation in the RMI system setup, two case studies were selected: The Pentecost storm (June 7-8-9 2014) and the storm of September 23-24-25 2012 which hit much of Western Europe.

As a first preliminary result (De Cruz et al. 2015), the assimilation of ZTDs yields a neutral to positive impact. For the Pentecost storm, the assimilation of SYNOP data + non-bias corrected ZTDs slightly improved the Root Mean Square Error (RMSE) and bias of the 2 m relative humidity (RH2m) for short (< 9 h) forecast range compared to SYNOP data only, as shown in Fig. 4.35. For the second case study, there is a neutral impact on the scores.
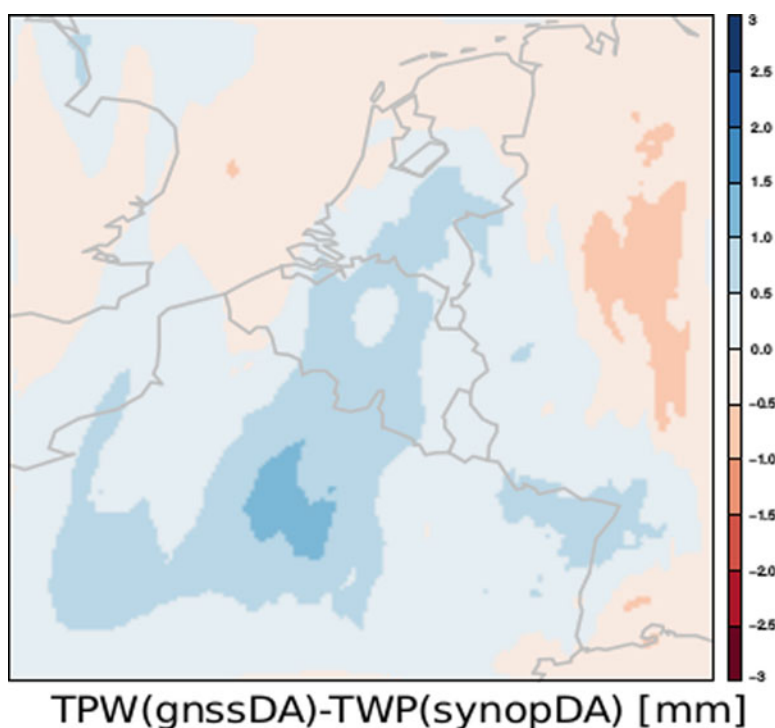
Fig. 4.34 Difference in Total Precipitable Water (TPW in mm) between a forecast with assimilated ZTDs versus a forecast in which only SYNOP data were assimilated.

While the preliminary results for the assimilation of non-bias corrected ZTDs are encouraging, it was found that applying a static bias correction largely cancels the positive effect of ZTD assimilation on the RH2m RMSE and bias. This may indicate that static bias correction currently represents the model biases rather than the biases present in the data (or representation difference), which effectively neutralizes the impact of the data assimilation. Possible causes are the overestimation of the ZTD observation errors with respect to the background (model) errors.

To solve the problems inherent to static bias correction, we intend to adopt variational bias correction, an algorithm to adaptively tune the background and observation error covariance matrix.

2m Relative Humidity RMSE (01–09 June 2014) run 0

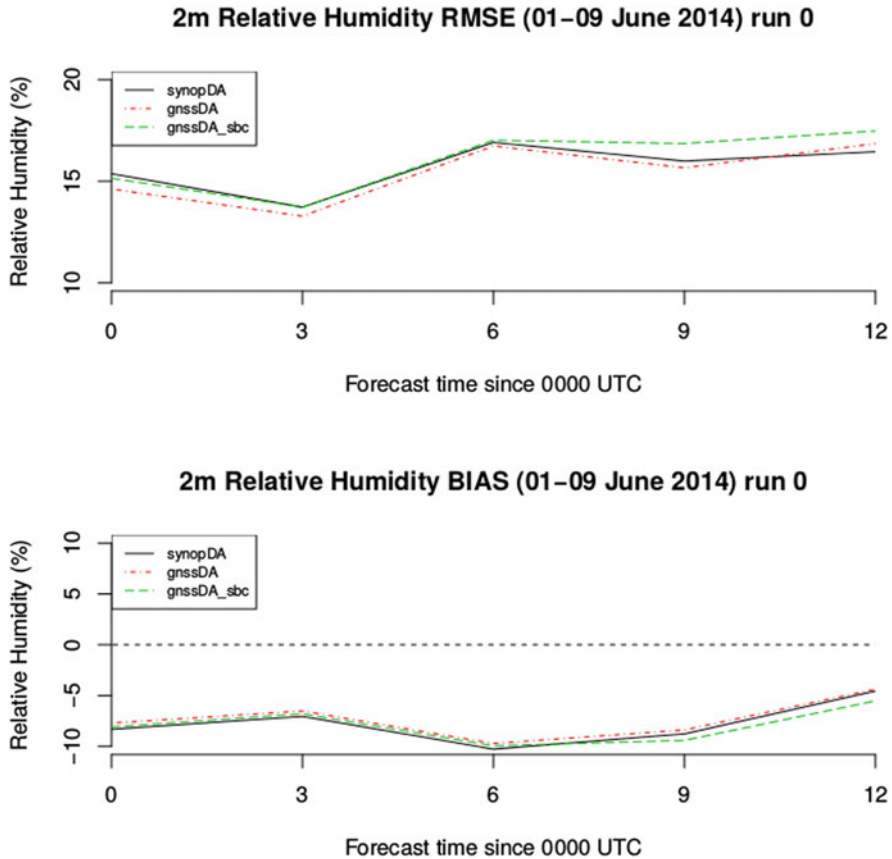## 2m Relative Humidity BIAS (01–09 June 2014) run 0

Fig. 4.35 RMSE (top) and bias (bottom) for the 2 m relative humidity during the case study of the Pentecost Storm of 2014

4.3.4 Slant Total Delay Assimilation in COSMO-DE: First Results

M. Bender
Deutscher Wetterdienst, Offenbach, Germany
e-mail: michael.bender@dwd.de

Slant total delays (STDs) provide directional information about the atmospheric state along the signal path between individual GNSS satellites and the receiver. Regarding the improved STD processing strategies described in Sect. 3.2, the assimilation of STDs into numerical weather models has the potential to supersede the assimilation of zenith total delays (ZTDs) which is currently operational at most European weather centres. In order to investigate the impact of STD assimilation into high-

resolution regional weather models the German Weather Service (DWD) developed a STD observation operator for COSMO/KENDA. This subsection gives a short description of the STD operator, the COSMO model and assimilation system and the current state of STD assimilation experiments at the DWD.

STD Observation Operator

The STD is defined by the difference between the optical path length of the GNSS signal in the atmosphere and the geometric distance G between satellite and receiver:

$$STD = \int_S n(s) \, ds - G \qquad (4.1)$$

The refractive index $n(s)$ along the signal path S depends on the temperature T, the pressure p and the relative humidity rh. The STD observation operator needs to evaluate this integral for a given atmospheric state, i.e. the 3D fields provided by a numerical weather model. The curved signal path S also depends on the atmospheric state and is not known in advance. The STD operator has to implement a ray tracer which estimates S, some interpolation from the discrete model fields on the signal path and the numerical integration of Eq. (4.1).

The ray tracer is the main component of the STD operator. It finds the signal path S by minimizing Eq. (4.1) and thereby evaluates the integral $\int n \, ds$. The raytracing algorithm used at the DWD is based on Fermat's principle, i.e. a variational approach for finding the minimum optical path length as described in (Zus et al. 2012, 2014). The minimization is done in a special Cartesian reference system linked to the satellite receiver axis. All required quantities, such as receiver positions, grid node coordinates, etc. are transformed to this reference frame assuming an ellipsoidal shape of the Earth. The curved signal path is approximated iteratively by computing the refractivities and their gradients along an estimated signal path which is refined in each iteration. The interpolation is done in three steps: (1) the refractivity is computed at adjacent grid nodes, (2) for each column the refractivities are vertically interpolated to the given height assuming an exponential profile, and (3) a bilinear horizontal interpolation provides the refractivity at the given point. A cubic four-point interpolation of unequally spaced data is used to approximate the integral in Eq. (4.1).

Validation of the STD Observation Operator

The new STD operator was tested using one month of operational COSMO-DE analyses and the latest STD product provided by the GFZ. For this test hourly analyses from March 2015 where read and the STD operator was running for all STD observations from that hour. The observation minus model statistics is shown in Fig. 4.36. In order to emulate the first guess check which removes "poor" observations from the assimilation all data with a relative difference greater than 1.5%, equivalent to about 3.5 cm in the zenith, were removed. In total 19,450,701 STDs were processed and $31,671 = 0.16\%$ were removed.
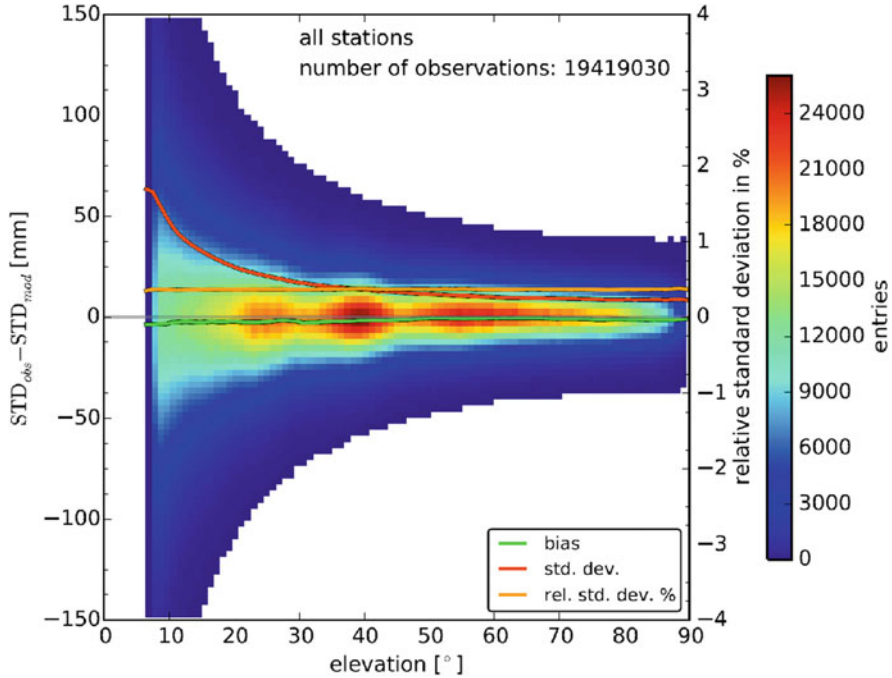
Fig. 4.36 Distribution of $STD_{obs} - STD_{mod}$ for all elevations ε. The variation of the bias (green line, mm) and the standard deviation (red line, mm) with the elevation is shown together with the relative standard deviation (orange line in %, right scale)

The 2D histogram in Fig. 4.36 shows a rather narrow distribution with a standard deviation of about 10 mm near the zenith ($\varepsilon \leq 90°$). At lower elevations $\varepsilon < 30°$ the standard deviation increases considerably up to about 65 mm. Such a behaviour could be expected as both the error of the processed STD data and the accumulated error of the weather model fields increase with decreasing elevation.

Altogether, the results were quite promising: The STDs from the new EPOS 8 version of the GFZ processing system show almost no bias with respect to the COSMO-DE model. The standard deviation is within the range of the expected STD observation error and the relative standard deviation is almost constant for all elevations down to 7°, which indicates, that neither the STD processing error nor the operator error increase disproportionally at low elevations.

COSMO: Model and Assimilation System

The DWD operates the limited-area numerical weather prediction model COSMO-DE (Baldauf et al. 2011) with a horizontal resolution of 2.8 km and 50 hybrid vertical layers up to 22 km. Hourly lateral boundary conditions are provided by the ICON global model with a global horizontal resolution of 13 km which is refined to 7.5 km over Europe. Observations are assimilated in an hourly cycle using an ensemble Kalman filter for convective-scale data assimilation (KENDA, Schraff

et al. 2016) which is based on a local ensemble transform Kalman filter (LETKF, Hunt et al. 2007). The operational COSMO-DE setup runs with an ensemble of 40 members and uses latent heat nudging of radar precipitation (Stephan et al. 2008).

The LETKF computes the analysis as a linear combination of the background ensemble where the weights of individual ensemble members depend on the differences between the observations and their model equivalents. The linear combinations are computed for each point of the analysis grid regarding all observations within the localisation radius. Currently, an analysis grid with 10 km horizontal resolution and 30 vertical layers is used. The LETKF approach is equivalent to propagating a flow dependent model error background covariance matrix.

First STD Assimilation Experiments

A number of STD assimilation experiments were executed in a quasi-operational environment, which emulates the full assimilation and forecast cycle of the operational COSMO-DE/KENDA system at the DWD. Conventional observations, such as synoptic data, radiosonde profiles, wind profiler data and aircraft observations were assimilated by the LETKF and the latent heat nudging was active during the COSMO-DE runs.

Some of these experiments showed promising results. One experiment for the period 17.5.–29.5.2014 showed a positive impact on the precipitation forecast validated with radar observations (Fig. 4.37). The equitable threat score (ETS) could be improved during the first 20 forecast hours which shows that the humidity information from the GNSS STDs makes a positive contribution to the model. However, the validation with other observations, especially radiosonde profiles, was slightly negative. In this experiment, the STDs were located at the GNSS station positions.

The processing of STDs with the LETKF leads to a fundamental problem with the assimilation of non-local observations with a local filter. The LETKF creates independent analyses for each point of the analysis grid, which requires observations with well-defined positions. Furthermore, the analysis depends on the differences $\delta y = y_o - H(x^b)$ at these points. In case of STDs it's not obvious what is the position of the STD and the observations represent the atmospheric state along the whole signal path without any information about local variations. Therefore, it is not optimal to assign δy to a certain point or set of points.

While there is no well-defined position of a STD it can be assumed that the position should be somewhere on the GNSS signal path. To select certain positions a reference height can be set within the STD operator. The operator estimates the position on the signal path with the given height and assigns the STD to that position. For a reference height of 0 m, all STDs will be located at the GNSS receiver positions, for increasing heights the horizontal STD positions will be shifted towards the GNSS satellite.
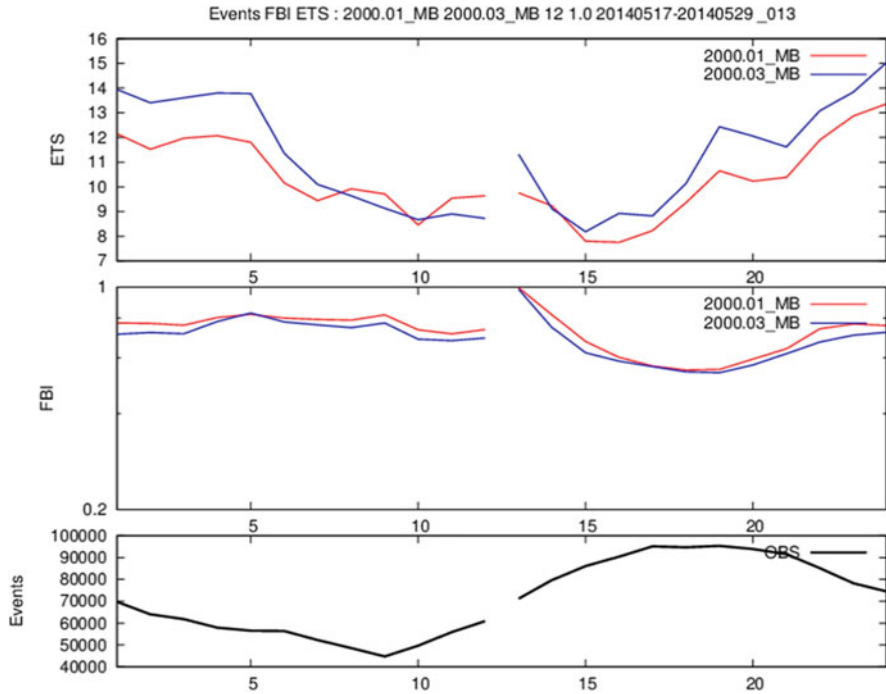
Fig. 4.37 Radar verification of precipitation, 17.5.–29.5.2014, 12:00 UTC forecasts, precipitation threshold 1 mm/h. The reference experiment (blue line) is compared with an STD assimilation experiment (red line). The equitable threat score (ETS), the frequency bias (FBI) and the total number of events (COSMO grid cells with rain) are shown

Another problem is the choice of the localisation radius. In the current implementation, the horizontal localisation radius defines a circle around the observation while the vertical localisation radius is a pressure range below and above the observations. There is no option to specify some direction, e.g. along the signal path.

To address this problem experiments with different STD positions and localisation radii were carried out and combined with different choices of the assumed STD error and of spatial and temporal thinning. The results are not yet consistent and work is in progress. However, it seems that a temporal thinning of the STD observations is necessary. STD observations with a sampling interval of 2.5 min, as provided by the GFZ, strongly outnumber all other observations and add up to more than 90% of all observations.

4.3.5   Data Assimilation Experiments with GNSS ZTD in AROME 3DVAR

M. Mile
Hungarian Meteorological Service, Budapest, Hungary
e-mail: mile.m@met.hu

At the Hungarian Meteorological Service (OMSZ) the use of GNSS ZTD is recognized as an important non-conventional observation source for local operational data assimilation (DA) systems. In the frame of GNSS4SWEC COST Action, DA studies were started in order to determine the impact of ZTD measurements on mesoscale AROME analyses and forecasts. During the first studies, observations from Hungarian E-GVAP network so called SGO1 have been evaluated and in latter studies, the observation set was extended with Czech GOP1 and Polish WUEL data as well. The domain of AROME and a typical distribution of GNSS ZTD observations for a particular case study are highlighted in the figures below (Figs. 4.38 and 4.39).

To assimilate GNSS ZTD a proper pre-selection of GNSS sites and an accurate bias correction have to be done. In the early studies, the pre-selection thresholds and static bias correction settings were employed after Poli et al. (2007) and Yan et al. (2008) in the Hungarian AROME 3D-Var assimilation system. The recent version of AROME DA consists only conventional observations (i.e. SYNOP, aircraft and radiosonde measurements) and the assimilation of ZTD on the top of conventional data showed positive impact on AROME winter skill and mostly neutral on summer forecasts. After these first encouraging results, the more advanced variational bias
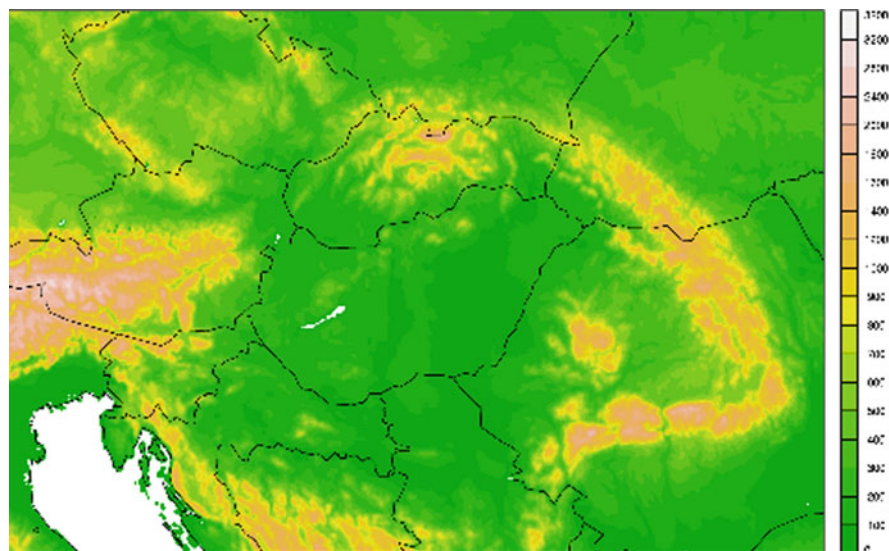

Fig. 4.38   The domain of mesoscale AROME NWP system at OMSZ

Fig. 4.39 Observation
status monitoring of GNSS
ZTD from SGO1, GOP1
and WUEL E-GVAP
networks for 12:00 UTC
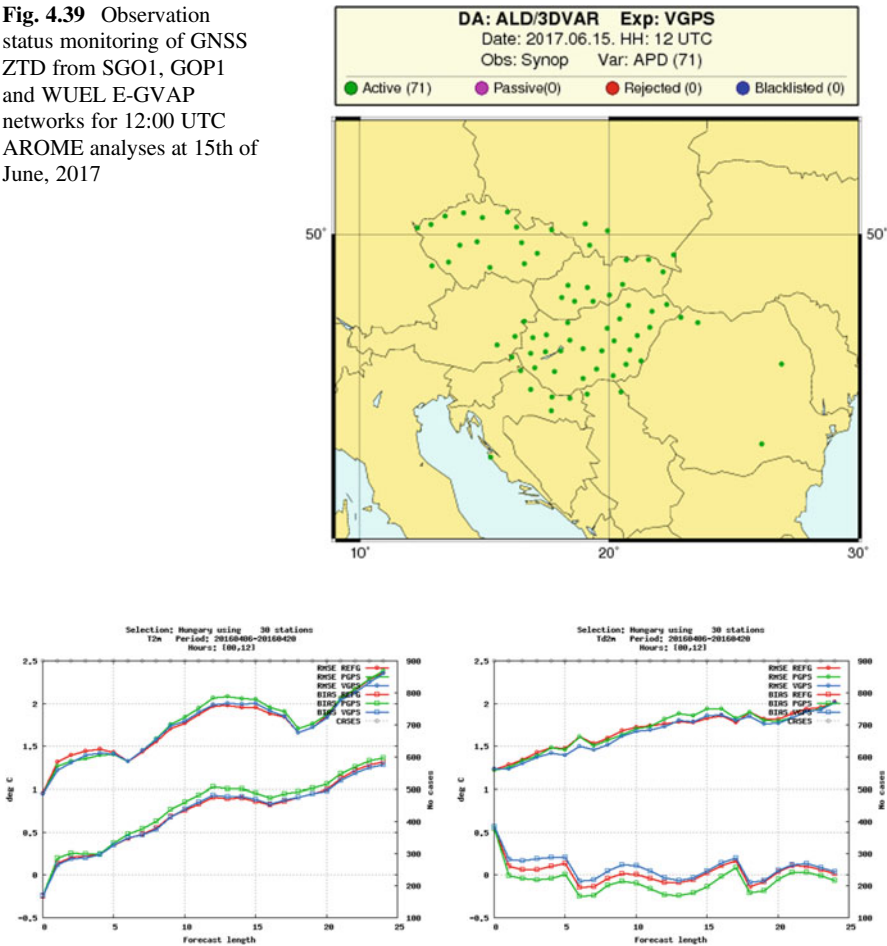AROME analyses at 15th of
June, 2017

Fig. 4.40 Assimilation impact study: RMSE and BIAS scores of AROME forecasts corresponding
to the operational AROME with conventional observations (REFG – red), AROME with conven-
tional plus GNSS ZTD based on static bias correction (PGPS – green) and AROME with
conventional plus GNSS ZTD based on variational bias correction (VGPS – blue) for 2 m
temperature and dew point temperature

correction (VARBC) approach (Sánchez-Arriola et al. 2016) was applied and tested
which provides adaptive bias correction better matched to the future needs of an
operational implementation. The benefit of the variational bias correction and the
assimilation of ZTD can be seen in Fig. 4.40 above.

The latest experiments included computation of optimal thinning distance
(~20 km), evaluation of the optimal VARBC predictor selection, observation mon-
itoring and diagnostic studies (Degree of Freedom for signal, etc.).

4.4 Tomography

W. Rohm
Institute of Geodesy and Geoinformatics, Wrocław University of Environmental and
Life Sciences, Wrocław, Poland
e-mail: witold.rohm@igig.up.wroc.pl

E. Trzcina
Institute of Geodesy and Geoinformatics, Wrocław University of Environmental and
Life Sciences, Wroclaw, Poland
e-mail: estera.trzcina@igig.up.wroc.pl

G. Möller
Department of Geodesy and Geoinformation, TU Wien, Wien, Austria
e-mail: gregor.moeller@geo.tuwien.ac.at

N. Dymarska
Department of Geodesy and Geoinformation, TU Wien, Wien, Austria
e-mail: natalia.dymarska@geo.tuwien.ac.at

H. Brenot
Royal Belgian Institute for Space Aeronomy, Uccle, Belgium
e-mail: hugues.brenot@oma.be

GNSS tomography is a novel technique that takes advantage of slant troposphere observations between GNSS receivers and satellites, traces these signals through the 3D grid of voxels and estimates through an inversion process the refractivity of the water vapour content within each voxel. The inversion is a highly variable and ill-posed process, hence the methodology to obtain reasonably well resolved troposphere field is a challenging task. The last 10–15 years of GNSS tomography development was focused on the numerical methods to stabilize the solution and get more out of the limited number of observations. As this has been achieved to the great extent, currently we are facing new challenges and possibilities for GNSS tomography in meteorology.

One of the key bottleneck limiting ingest of slant troposphere observations in numerical weather prediction models is a large number of numerical operations required to calculate model-based slants. Additionally, there is a great debate within meteorologists' society as to how assign uncertainty of the slant or zenith delay measurements. The measurement is taken at the station location but the quantity is measured along some trajectory. Using GNSS tomography methodology one can estimate refractivity or water vapour content in a 3D grid with full variance-covariance matrix, which can be used directly in the assimilation process.

On the other hand, same information, i.e. 3D water vapour distribution, but delivered in Near Real-Time or Real-Time using batch processing or stream processing could be another data source for forecasters as an additional tool for assessing

precipitable water content over area covered by the GNSS network. This might be of
benefit e.g. in cases with moist unstable air being advected over the domain of interest.

4.4.1 Nowcasting Using Tomography

Severe weather is a growing threat to people and infrastructure all around the world,
in Europe the most common event is extensive and prolonged precipitation that may
cause a large scale flooding. This weather type is associated with widespread
precipitation caused by the convergence on macro scale of air masses in cyclonic
systems. Extreme widespread rainfall triggered by convergence on macro scale 5 are
usually formed as a result of intensive cyclogenesis organized in the form of quasi-
stationary thermal asymmetric appearing from the low barometric pressure of the
southern sector of the Central Europe. Such low barometric pressure provides power
in moist air from the sector from S through SE and E to NE, which ascends over the
cold air coming from the sector NW and N. Frontal surface separating two air masses
is predominantly anabatic cold front. As such events are very well studied in
literature and predicted to the great extent with sufficient accuracy, we decided to
apply GNSS tomography model TOMO2 to resolve the water vapour content before,
during and after the event. The applied technique allows getting full picture of
troposphere at all locations covered by GNSS network. In this study, we investigate:
(1) the meteorological correctness of the tomography retrieval, (2) whether the new
temporal and spatial resolution of the troposphere water vapour content will provide
new information regarding these well studied events. Two events were investigated:
one in May 2014 and one in August/September 2014, the tomography retrievals are
compared with radiosonde profiles and numerical weather prediction (NWP) model.
We show better agreement of tomography data with radiosonde data than NWP has
with radiosonde, we also show the intersections through the cold front and associ-
ated atmosphere profile variability. The overall picture of water vapour supply to the
rain bands locations is also well represented.

4.4.2 Requirements for Assimilation of Tomography Results

After discussion with Met Office experts following requirements in regards to the
troposphere profiles retrieved from tomographic models (Table 4.3) were established.

   The criteria set up by Met Office experts are quite tight especially as to what
vertical resolution of tomography model retrievals they are interested in. The tomog-
raphy profile quality is a function of interstation distance, terrain undulation, STDs
quality and as such, it is rather infrastructure dependent. Currently the European
reference network does not provide enough station density to achieve such high
standard results of tomography retrieval over the whole domain, therefore we
propose to use limited area models.

Table 4.3 The set of requirements that tomographic retrieval should fulfil in order to be assimilated in the NWP models

Parameter	Requirements minimum (target)
Number of horizontal layers	16 (20)
Bottom layer	<2.0 km (0.5 km)
Top layer	6 km
Inversions	Resolved
Height difference between receivers	~300 m (1000 m)
Distance between receivers	<20 km
Cut-off angle	5 deg. (1.4 deg)
Bending impact	Resolved 59 mm (2397 mm)

According to Seidel et al. (2010) the radiosonde balloon mean drift w.r.t. the pressure levels (approx. height) in the northern hemisphere mid latitude is as follows: 850 hPa (~1500 m) – 2 km, 700 hPa (~3200 m) – 5 km, 500 hPa (~5800 m) – 10 km 300 hPa (~9500 m)- 20 km, 100 hPa (~16,000 m) – 55 km. Therefore, it puts another constraint of 10 km voxel size in the bottom part of the troposphere. Ascend time for radiosonde is 5 min to 2 km and 1.5 h to the top of the troposphere, thus the maximum integration time for tomography should not exceed 1 h.

4.4.3   Assimilation of Relative Humidity

For assimilation purposes, a tomography dataset was provided with one-hour temporal resolution for the first two weeks in April 2016. The tomography model covers the area from 14.2° E to 23.8° E (grid point every 0.8°) and 49.25°N to 54.75° N (grid point every 0.5°), including nine height levels (290, 790, 1290, 1790, 2290, 2790, 3790, 5290 and 6790 m).

The assimilation itself was carried out using the Weather Research and Forecasting Data Assimilation System (WRFDA). WRFDA was configured using two nested domains with a spatial resolution of 12 km × 12 km (259 × 282 grids) and 4 km × 4 km (238 × 220 grids, Fig. 4.41), respectively. Vertically, all domains have 48 levels. Data from the Global Forecasting System (GFS) are used as initial and boundary conditions, available every 6 h. WRFDA allows using both 3D and 4D data assimilation. Here we have used a 3D data assimilation approach (3DVAR). 3DVAR is a variational method based on minimization of a cost function. For assimilation of tomography data, the WRFDA standard observation operator for upper air sounding was applied. Therefore, the wet refractivity fields as obtained from the tomography solution, were converted into time series of relative humidity (in %).

The forecast was started at 00:00 UTC for each day the period covered with TOMO data (01.04.2016–14.04.2016). The lead time was 48 h and meteorological information was written every 1 h to the output file for further post processing. Both

Fig. 4.41 WRF model domains and terrain elevation (msl)
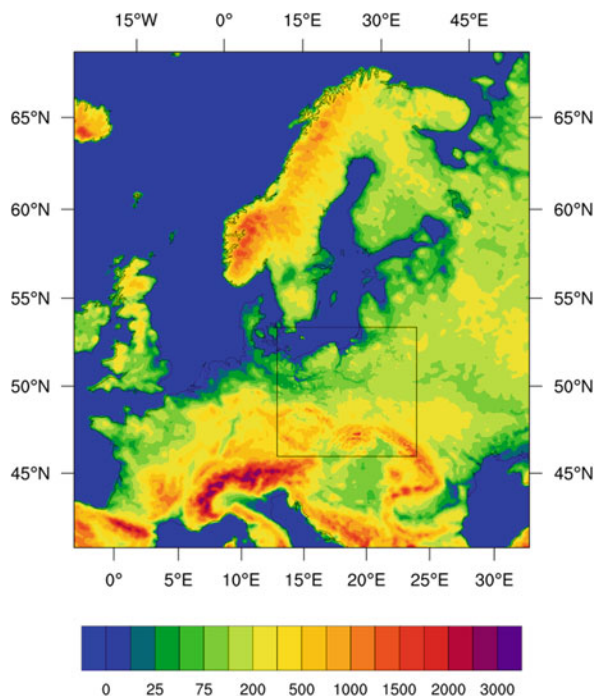
runs (base run and with TOMO data assimilated for the nested domain) were compared to quantify the differences. The differences were calculated for air temperature at 2 m (T2), mixing ratio at 2 m (Q2), rainfall (RAIN; accumulated since the first hour of the model run) and wind speed at 10 m.

Figure 4.42 presents the forecast started at 01.04.2016 00:00 UTC, lead time 6 h, for air temperature at 2 m and accumulated rainfall. There are significant differences in spatial distribution of both meteorological variables. The largest differences between the base run and the model run with TOMO data assimilated are obtained close to the front line. For air temperatures, the differences exceed +/− 2 K. For the majority of the model domain area, air temperatures at 2 m are higher for the base run than for the TOMO assimilation run. For rainfall (accumulated for 6 h) the differences exceed 10 mm.

Verification of the temperature measurements indicate a mixed negative and positive impact (Fig. 4.43) which should be linked with very long assimilation window (13 h) of a fast changing parameter (RH).

4.4.4 Assimilation of Temperature and Specific Humidity

For tomography assimilation studies at the Central Institute for Meteorology and Geodynamics (ZAMG), Austria, May and June 2013 were selected as study period.
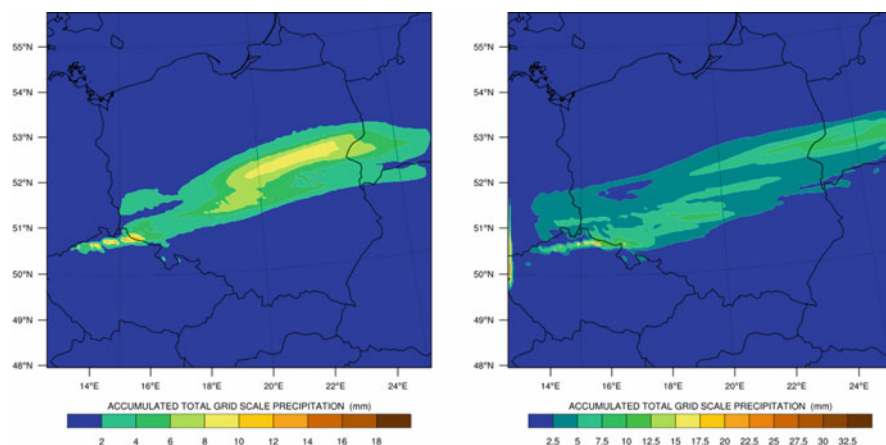
Fig. 4.42 Forecasted accumulated rainfall for the model run without data assimilation left and with data assimilation right. Forecast start time 01.04.2016 00:00 UTC, lead time 6 h
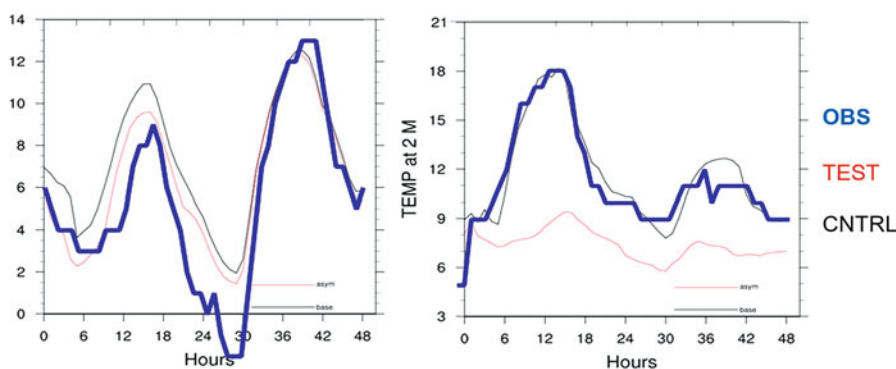

Fig. 4.43 Forecasted temperature for the model run without data assimilation (black line), with data assimilation (red line), against observations at the EPWR station (blue line). For 01.04.2016 + 48 h left and 07.04.2016 + 48 h right.

Within this period, a series of extratropical cyclones of type 'Vb' (Grams et al. 2014) with origin in the Mediterranean and South-East Europe brought very moist and warm air around the Alps, which finally caused a century flood event, affecting the Danube and Elbe catchment areas. Especially end of May and beginning of June INCA precipitation analysis (Möller et al. 2016) revealed heavy precipitation events, with up to 300 mm accumulated precipitation in 72 h over South-East Germany and Austria.

In order to study the atmospheric processes within this period more in detail, a tomography dataset was computed over the entire period of two months with three-hour temporal resolution. The resulting wet refractivity fields reflect the atmospheric
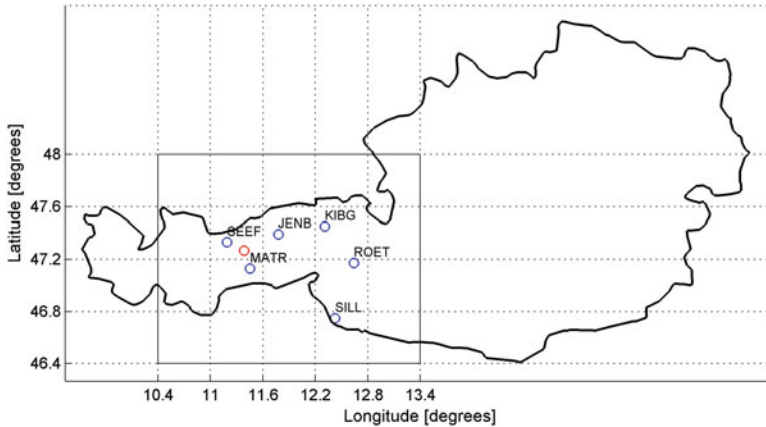
Fig. 4.44 Voxel model and GNSS station distribution in Western Austria. The red circle indicates the location of the radiosonde launch at Innsbruck airport

conditions within the area of Western Austria, parts of Germany and Italy, see Fig. 4.44. For more details about the tomography processing strategy, the reader is referred to (Möller 2017).

Comparisons with radiometer data at Innsbruck airport reveal that the tomography solution, i.e. the obtained wet refractivity fields are significantly less biased than operational numerical weather model data (ALARO), see Fig. 4.45. In consequence, during the assimilation tests a significant impact on the forecast field, especially on the vertical structure of the humidity field is expected.

The assimilation itself was carried out at ZAMG by setting up an extended observation system simulation experiment. Over a period of 14 days (23.05.–05.06.2013) the operational AROME model (2.5 km horizontal resolution, 48 h integration time) was driven with a basic set of conventional and non-conventional observations. On top of this basic setup, different assimilation tests were performed, including the assimilation of ZTDs and wet refractivities.

In contrast to previously described assimilation runs, the wet refractivity fields were transformed into profiles of specific humidity and temperature using a 1DVAR approach, which could be assimilated as conventional T, q-profiles into AROME using a 3DVAR approach. In total 112 AROME model runs had to be performed and evaluated. From this runs we have seen that assimilation of refractivity tends to have a drying effect on the AROME forecast, especially at lower atmospheric levels.

For further analysis, the amplitude score was computed for each model run. This score evaluates the quality of area mean precipitation forecasts with respect to gridded observation data (which is INCA in our case). An A score of '0' would indicate a perfect correspondence between forecast and observation date while values <0 can be interpreted as underestimation and values >0 as overestimation by the model.
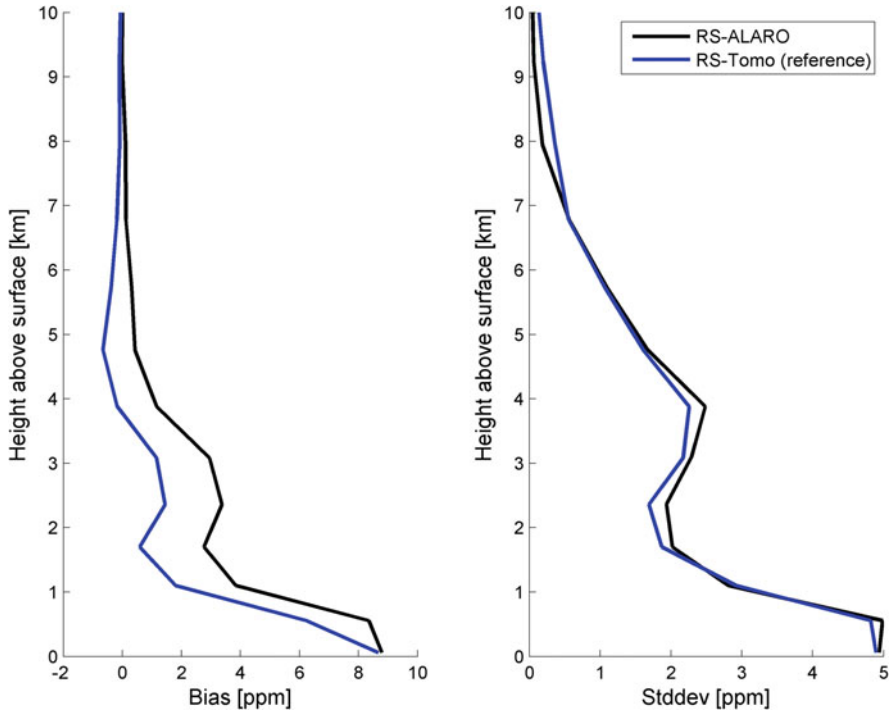
Fig. 4.45 Statistic of the comparison of ALARO and tomography derived wet refractivities with radiosonde profiles. Analysed period: May 2013

Figure 4.46 shows the amplitude score for various assimilation scenarios. It clearly shows that the experiment runs using refractivity observations in the assimilation (ZG02 and ZG04) produce significantly less precipitation than the reference run (ZG01) and the runs using ZTD observations during the first 9 or even 12 h of the forecast (ZG03 and ZG05). According to the amplitude score, the bias correction of ZTD data tends to decrease precipitation in early forecast hours, this gets visible when comparing ZG03 and ZG05.

From the results, we can assume that applying a (variational) bias correction might reduce the amplitude of the drying effect and decrease the overall impact of this observation type. Overall, the results of these assimilation tests clearly show the potential of 3D refractivity observations.

4.4.5 Assimilation of Wet Refractivity

For the described test case, a tomography dataset was derived from slant wet delays, observed at 72 GNSS sites in Eastern Germany and parts of Czech Republic in May and June, 2013. Therefore, the same tomography processing strategy was applied as
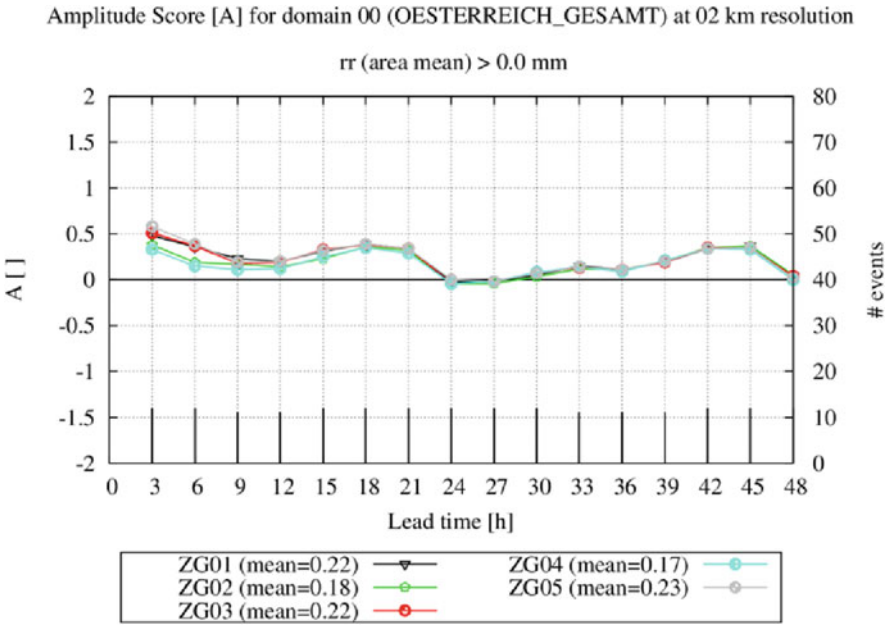
Amplitude Score [A] for domain 00 (OESTERREICH_GESAMT) at 02 km resolution

Fig. 4.46 Mean amplitude score (A) as a function of forecast lead time

described in the previous subsection using the ATom tomography package, which was developed at TU Wien. For the assimilation, the Weather Research and Fore-casting Data Assimilation System (WRFDA) was configured for the area of Central Europe (Fig. 4.47) with 36 km horizontal spacing and 35 vertical levels. The model top was defined at 50 hPa air pressure.

In total a one-day long assimilation experiment was performed, with (GPS NW) and without (CTRL) GNSS tomography product assimilation. Thereby two solutions were tested: (1) assimilation of relative humidity profiles, (2) assimilation of refrac-tivity observations. The WRF model background (initial and boundary conditions) was derived from NCEP FNL (final) operational global analysis data with $1° \times 1°$ horizontal resolution and 26 vertical layers. In case of assimilation, the model is started at 06:00, 12:00 and 18:00 UTC and is integrated for 6 h (so-called cycle-mode). After that, refractivity fields are applied to the 6-h forecast field through WRF 3DVAR assimilation with a 3-h time window.

For evaluation of the assimilation results, comparisons with radiosonde data were carried out. Figure 4.48 shows the obtained vertical profiles of relative humidity and wind speed, exemplary for RS stations 12,425 and 10,184.

The correlation coefficients (R) between RS and WRF forecasted relative humidity (RH), wind speed (WS) and temperature (T) are summarized in Table 4.4. While in terms of temperature, the correlation remains close to one, the correlation of the relative humidity profiles increased after assimilation of the refractivity fields, from 0.52 to 0.65 (10184), or 0.77 to 0.81 (10393). In contrast

Fig. 4.47 CASE2 WRF model domain including the locations of the radiosonde stations used for model evaluation

the correlation of wind speed decreased after assimilation from 0.78 to 0.75 (10184). This is probably related to the dry part of refractivity, which was added for assimilation purposes.

4.4.6 Conclusions

In conclusion, the assimilation of the tomography outputs into WRF DA is possible using available modules, dedicated for other observations. Two solutions were tested: (1) assimilation as relative humidity profiles, (2) assimilation as refractivity observations.

In case 1, the results show that the impact of GNSS tomography data assimilation on meteorological forecast is significant. Large changes were observed for air temperature at 2 m, mixing ratio at 2 m, rainfall and wind speed. The impact of data assimilation varies spatially and changes with general synoptic situation. Data assimilation strongly affects first 24 h of the forecast, but for several cases it was also significant for the entire forecast (48 h).

In case 2, larger changes in the initial conditions of the model appear and a noticeable, positive impact on the relative humidity forecasts is obtained.
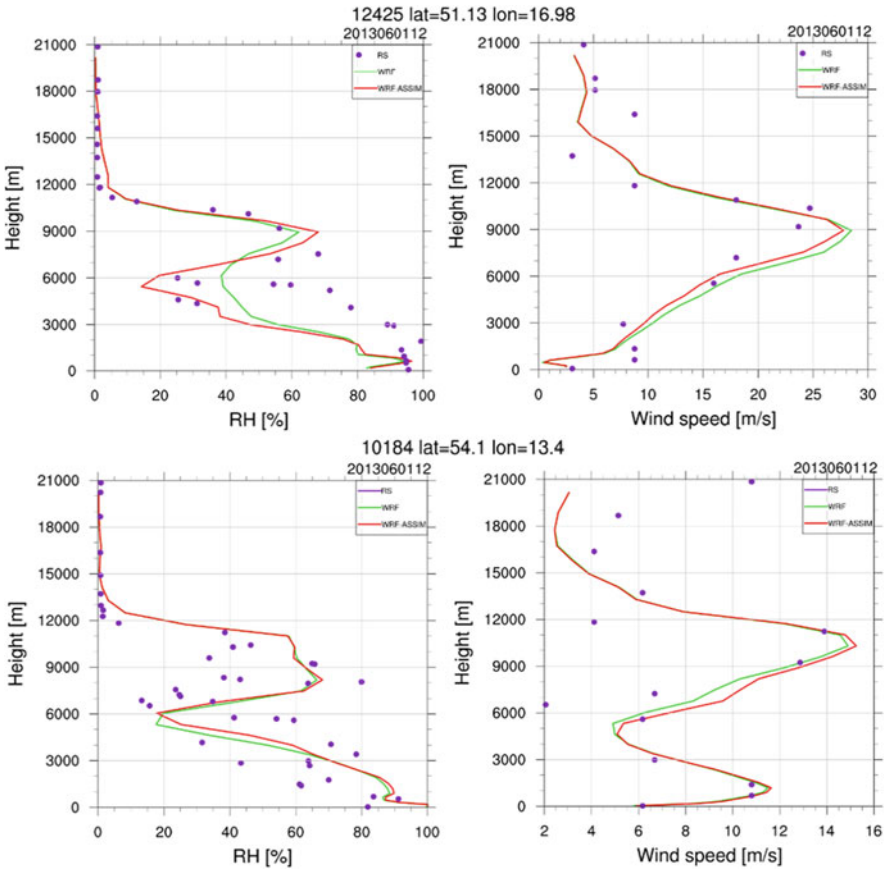
Fig. 4.48 The profiles of the relative humidity (left) and the wind speed for RS (purple) and WRF (red – after refractivity assimilation, green – control dataset) data. Plots for 12,425 (top) and 10,184 (bottom) RS stations

Table 4.4 Correlation between RS and WRF data for 5 RS stations. Date time is 2013-06-01 12:00 UTC

	R [%]					
	RH		WS		T	
Station	CTRL	after assim.	CTRL	after assim.	CTRL	after assim.
10,184	0.58	0.62	0.78	0.75	1.00	1.00
12,120	0.45	0.49	0.88	0.86	1.00	1.00
10,393	0.77	0.81	0.76	0.69	1.00	1.00
12,425	0.93	0.88	0.89	0.90	1.00	1.00
11,520	0.84	0.78	0.88	0.82	1.00	1.00
11,035	0.70	0.71	0.92	0.88	1.00	1.00
11,952	0.86	0.88	0.46	0.44	1.00	1.00
mean	0.73	0.74	0.79	0.76	1.00	1.00

4.5   Benchmark and Case Study Databases at the U.K. Met Office

J. Jones
Met Office, Exeter, UK
e-mail: jonathan.jones@metoffice.gov.uk

This sub-WG was established to define and generate specific benchmark datasets in the form of GNSS observations, alternative water vapour and refractivity observations, and NWP products, for test, assessment and validation for each method/product in conjunction with WG1. Only by validation of traditional and more advanced GNSS tropospheric products (developed in WG1) will the scientific community (specifically the forecasting community) have a better understanding of the benefit of GNSS-tropospheric products to meteorology.

Benchmark Campaign

During the first year of the Action, a benchmark area/time period was determined for the testing and validation of advanced GNSS tropospheric products and processing algorithms developed by WG1. After consideration of a number of areas and events, it was determined that the benchmark campaign should be focused on the areas of Germany/Poland (with some data from surrounding countries) which suffered extremely heavy precipitation in the period of May–June 2003, causing severe flooding of the Danube, Moldau and Ebla rivers.

A database was established at the Geodetic Observatory, Pecny, Czech Republic in conjunction with the International GNSS Service, which met the requirements of the benchmark database, (http://www.pecny.cz/gop/index.php/gop-tropdb). The database contains the following datasets:

- GNSS: ~500 stations, SYNOP: ~200 stations
- NWM: regional (Aladin-CZ), global (ERA-Interim, NCEP GFS)
- RAOBS: 2 high-resolution
- WVR: Potsdam, Lindenberg
- RADAR images: Brdy, Skalka

- Reference products
- GNSS: Bernese (GOP), EPOS (GFZ)
- NWP: G-Nut/Shu (GOP), DNS (GFZ)

More information on the benchmark campaign can be found in detail in subsection 4.1.1 of this report.

Severe Weather Case Study Database

A database was established on a publicly-facing ftp server at the UK Met Office (ftp.metoffice.gov.uk) for the collection and ditribution of severe weather case studies. The case studies uploaded to the database are those found in Sect. 4.2 of this Report plus additional severe weather case studies from events in Austria, Czech Republic, Italy, Lithuania, the Netherlands and the UK.

The database will be supported long-term for the benefit of scientific research and forecaster use. The database is user/password controlled, so please contact jonathan.jones@metoffice.gov.uk for access.

NWP Database for Input to GNSS Processing

This task was created to establish and feed a database with live meteorological data to be used as an input to real-time GNSS positioning. ZTD estimates rely on mapping functions to estimate the atmospheric condition. Advance knowledge of the atmosphere can not only lead to more realistic ZTD and IWV estimates, but also improve GNSS convergence time, thus aiding the positioning community.

The creation of a database at the UK Met Office for the provision of live (i.e. real-time) NWP unified model (UM) output to aid real-time positioning was unfortunately not possible due to UM licence restrictions. Whilst providing the GNSS community with live data was not possible, the provision of offline data for post-processing applications was possible. As is documented in subsection 3.4.10 of this report, a European Space Agency (ESA) funded project, 'RTTSD – Validation and Implementation of Direct Tropospheric Delay Estimation for Precise Real-Time positioning' was established between the University of Nottingham (UoN) and the Met Office, whereby the UoN used data from the Met Office UM model (accessible via the British Isles Atmospheric Data Centre (BADC)), as an input to real-time PPP processing to improve GNSS solution convergence time, with the longer-term view of providing industry with a GNSS quality flag warning system. Please see subsection 3.4.10 for more details.

Additional data for future studies should be requested on a case-by-case basis to the UK Met Office.

4.6   ZTD to IWV Conversion

UK Met Office Operational conversion of ZTD to IWV

J. Jones
Met Office, Exeter, UK
e-mail: jonathan.jones@metoffice.gov.uk

At the UK Met Office, IWV is derived from ZTD using surface meteorological observations retrieved from the Met Office database, the MetDB. On an hourly or sub-hourly basis (determined by the frequency of the GNSS processing system), the database is interrogated and meteorological parameters for all 8000+ global surface sites are extracted. The parameters are; site identifier, latitude, longitude, height, date, time, temperature, dew point temperature and MSL pressure.

Latitude and longitude are read into a MySQL database and values are compared against the latitude and longitude of the GNSS sites used for that particular processing campaign, and thus meteorological data from the nearest surface-

observing site to each GNSS site is chosen. If data from the nearest site is not available, then the next nearest site's data is used, and so on. The temperature and dew point temperature are used as-is, but the MSL pressure must be converted to the pressure at the GNSS antenna height using the formula of Saastamoinen (1972).

In an ideal world, high quality pressure and temperature sensors would be collocated alongside the GNSS antennae, however this is not practical in reality primarily in terms of the cost and infrastructure requirements. Using the nearest sites' pressure is generally deemed adequate as pressure fields do not vary greatly in the horizontal on the scales in this scenario (generally <40 km), however care must be taken as a 1 hPa pressure error typically leads to errors in IWV of around 0.4 km/m^2. For reference, 1 °C temperature error typically leads to an error of around 0.1 km/m^2 in IWV.

Additionally, the forecast field of a rapid-cycle NPW model could be used to obtain the parameters necessary for ZTD to IWV conversion, and this could be an interesting option to investigate further in the future.

GFZ

G. Dick
GFZ German Research Centre for Geosciences, Helmholtz Centre Potsdam, Potsdam, Germany
e-mail: dick@gfz-potsdam.de

F. Zus
GFZ German Research Centre for Geosciences, Potsdam, Germany
e-mail: zusflo@gfz-potsdam.de

For conversion of the adjusted ZTD into the integrated water vapour (IWV), the meteorological surface data at the stations is needed (the pressure for getting the zenith wet delay; the temperature profile, approximated by linear regression from surface data). For some stations, e.g. the 24 GFZ-DWD sites, local measurements are available. However, for most of the sites the needed pressure and temperature have to be interpolated using the synoptic sites of the DWD (about 200 sites with hourly sampling rate of data). For each site, the smallest surrounding station triangle is used for a linear interpolation, correcting for the height differences beforehand. Stations with a height over 1000 m are excluded because of limitations of interpolation accuracy caused by errors in height correction. The quality of the interpolation is normally 0.3 hPa (RMS). In mountainous regions, the error can reach higher values, but 0.5–1 hPa (corresponding to about 0.2–0.4 mm IWV) can be accepted for numerical weather prediction if these are only random fluctuations, however, there are only a few sites that do not meet this limit. The pressure data are checked beforehand by mutual interpolation to eliminate sites, which can be regarded as outliers in the pressure field over Germany. That means, each pressure value is compared to the interpolated value using surrounding sited, and it is excluded if the difference exceeded given accuracy limit.

Additionally, in the case that pressure and temperature observations are not available (e.g. the meteorological sensors are not co-located) the pressure and

temperature values can be obtained from Numerical Weather Model (NWM) data. Since the grid points of the NWM are not co-located with the GPS stations, pressure and temperature values are obtained by interpolation utilizing the nearest grid points.

Further Reading

The empirical conversion of ZTD to IWV is covered in subsect. 1.2.4. A review of conversion methods with a view of determining a climatological standard are covered in subsect. 5.4.2.

References

Askne, J., & Nordius, H. (1987, May–June). Estimation of tropospheric delay for microwaves from surface weather data. *Radio Science*, *22*(3), 379–386. https://doi.org/10.1029/RS022i003p00379.

Baldauf, M., Seifert, A., Förstner, J., Majewski, D., Raschendorfer, M., & Reinhardt, T. (2011). Operational convective-scale numerical weather prediction with the COSMO model: Description and sensitivities. *Monthly Weather Review, 139*(12), 3887–3905.

Bennitt, G. V., & Jupp, A. (2012). Operational assimilation of GPS Zenith total delay observations into the Met office numerical weather prediction models. *Monthly Weather Review, 140*, 2706–2719.

Bevis, M., Businger, S., & Herring, T. (1992). GPS meteorology: Remote sensing of atmospheric water vapour using the Global Positioning System. *Journal of Geophysical Research: Atmospheres, 97*(D14), 15787–15801. https://doi.org/10.1029/92JD01517.

Bevis, M., Businger, S., Chiswell, S., Herring, T., Anthes, R., Rocken, Ch., & Ware, R. (1994, March). GPS meteorology: Mapping zenith wet delays onto precipitable water. *Journal of Applied Meteorology and Climatology*, *33*(3), 379–386. https://doi.org/10.1175/1520-0450(1994)033%3C0379:GMMZWD%3E2.0.CO;2.

Bruyninx, C., Habrich, H., Söhne, W., Kenyeres, A., Stangl, G., & Völksen, C. (2012), Enhancement of the EUREF permanent network services and products. In *Geodesy for planet Earth*, vol. 136 of IAG symposia series (pp. 27–35). Springer.

Caumont, O., Ducrocq, V., Wattrelot, É., Jaubert, G., & Pradier-Vabre, S. (2010). 1D+3DVar assimilation of radar reflectivity data: A proof of concept. *Tellus A, 62*, 173–187.

Chen, G., & Herring, T. (1997, September). Effects of atmospheric azimuthal asymmetry on the analysis of space geodetic data. *Journal of Geophysical Research: Solid Earth*, *102*(B9), 20489–20502. https://doi.org/10.1029/97JB01739.

Dach, R., Lutz, S., Walser, P., & Fridez, P. (Eds) (2015). *Bernese GNSS Software Version 5.2. User manual*. Astronomical Institute, University of Bern, Bern Open Publishing. https://doi.org/10.7892/boris.72297. isbn:978-3-906813-05-9.

Davis, J., Herring, T., Shapiro, I., Rogers, A., & Elgered, G. (1985, November–December). Geodesy by radio interferometry: Effects of atmospheric modelling errors on estimates of baseline length. *Radio Science, 20*(6), 1593–1607. https://doi.org/10.1029/RS020i006p01593.

De Cruz, L., & Duerinckx, A.(2015, April 13–16). *Assimilation of GNSS and radar data in ALARO cy38t1 at RMIB*. Joint 25th ALADIN Workshop & HIRLAM All Staff Meeting, Helsingor, Denmark.

De Cruz, L., Duerinckx, A., & Pottiaux, E. (2015, May 11–13). *GNSS assimilation in NWP: Case studies for Belgium*. COST ES1206 – GNSS4SWEC: 2nd Workshop, Thessaloniki, Greece.

De Haan, S., Barlag, S., Klein Blatink, H., Debie, F., & van der Marel, H. (2004, April). Synergetic use of GPS water vapour and meteosat images for synoptic weather forecasting. *Journal of Applied Meteorology and Climatology*, *43*(3), 514–518. https://doi.org/10.1175/1520-0450(2004)043%3C0514:SUOGWV%3E2.0.CO;2.

De Haan, S., Holleman, I., & Holtslag, A. (2009). Real-time water vapour maps from a GPS surface network: Construction, validation, and applications. *Journal of Applied Meteorology and Climatology, 48*(7), 1302–1316. https://doi.org/10.1175/2008JAMC2024.1.

E-GVAP PDR. (2010, December 21). *Product requirements document v 1.0*. Prepared by the Met Office. http://egvap.dmi.dk/support/formats/egvap_prd_v10.pdf

Elgered, G., Davis, J., Herring, T., & Shapiro, I. (1991, April). Geodesy by radio interferometry: Water vapour radiometry for estimation of the wet delay. *Journal of Geophysical Research – Solid Earth 96*(B4), 6541–6555. https://doi.org/10.1029/90JB00834.

Grams, C. M., Binder, H., Pfahl, S., Piaget, N., & Wernli, H. (2014). Atmospheric processes triggering the central European floods in June 2013. *Natural Hazards and Earth System Sciences, 14*(7), 1691–1702.

Guerova, G. (2013). Ground-based GNSS Meteorology: Case studies for Bulgaria/Southeast Europe. In *Proceedings of the 4th International colloquium – Scientific and fundamental aspects of the Galileo programme*, Prague, Czech Republic, 4–6.12.2013. http://suada.phys. uni-sofia.bg/wordpress/wp-content/uploads/2015/02/2923524_guerova.pdf

Heise, S., Dick, G., Gendt, G., Schmidt, T., & Wickert, J. (2009). Integrated water vapour from IGS ground-based GPS observations: Initial results from a 5-min data set. *Annales de Geophysique, 27*, 2851–2859. https://doi.org/10.5194/angeo-27-2851-2009.

Hogg, D., Guiraud, F., & Decker, M. (1981). Measurement of excess transmission length on Earth–space paths. *Astronomy and Astrophysics, 95*, 304–307.

Holton, J. R. (1972). *An introduction to dynamic meteorology* (p. 319). New York: Academic.

Hunt, B. R., Kostelich, E. J., & Szunyogh, I. (2007). Efficient data assimilation for spatiotemporal chaos: A local ensemble transform Kalman filter. *Physica D: Nonlinear Phenomena, 230*(1–2), 112–126.

Lindskog, M., Ridal, M., Thorsteinsson, S., & Ning, T. (2017). *Data assimilation of GNSS Zenith Total Delays from a Nordic processing centre*. Submitted to Atmospheric Chemistry Physics.

Matheron, G. (1962). *Traité de géostatique appliquée.* Tome I, Mémoires du Bureau de Recherche Géologiques et Minières, N°14, Edt. Technip, Paris.

Matheron, G. (1963a). Principles of Geostatics. *Economic Geology, 58*(8), 1246–1266. https://doi.org/10.2113/gsecongeo.58.8.1246.

Matheron, G. (1963b). *Traité de géostatique appliquée*. Tome II: le Krigeage, Mémoires du Bureau de Recherche Géologiques et Minières, N°24, Edt. B. R. G. M., Paris.

Mazany, R., Businger, S., & Gutman, S. (2002, October). A lightning prediction index that utilizes GPS integrated precipitable water vapour. *Weather and Forecasting*, *17*, 1034–1047.

Möller, G. (2017). *Reconstruction of 3D wet refractivity fields in the lower atmosphere along bended GNSS signal paths*. Dissertation, TU Wien, Department of Geodesy and Geoinformation, 211p.

Möller, G., Wittmann, C., Yan, X., Umnig, E., Joldzic, N., & Weber, R. (2016). *3D ground based GNSS atmospheric tomography*. Final Report GNSS-ATom project 840098, 49p.

Muller, M., Homleid, M., Ivarsson, K.-I., Koltzow, M., Lindskog, M., Midtbo, K.-H., Andrae, U., Aspelien, T., Berggren, L., Bjorge, D., Dahlgren, P., Kristiansen, J., Randriamampianina, R., Ridal, M., & Vigne, O. (2017). AROME-MetCoOp: A nordic convective-scale operational weather prediction model. *Weather and Forecasting, 32*, 609–627. https://doi.org/10.1175/WAF-D-16-0099.1.

Ning, T., Elgered, G., Willén, U., & Johansson, J. (2013). Evaluation of the atmospheric water vapour content in a regional climate model using ground-based GPS measurements. *Journal of Geophysical Research: Atmospheres, 118*(2), 329–339. https://doi.org/10.1029/2012JD018053.

Poli, P., Moll, P., Rabier, F., Desroziers, G., Chapnik, B., Berre, L., Healy, S. B., Andersson, E., & El Guelai, F.-Z. (2007). Forecast impact studies of Zenith total delay data from European near real-time Gps stations in Météo France 4DVAR. *Journal of Geophysical Research: Atmospheres*, *112*(D6). Wiley Online Library.

Pottiaux, E. (2010). *Sounding the Earth's atmospheric water vapour using signals emitted by global navigation satellite systems*. PhD. thesis in Sciences, 200. Université Catholique de Louvain.

Rocken, C., Van Hove, T., Johnson, J., Solheim, F., Ware, R., Bevis, M., Chiswell, S., & Businger, S. (1995), GPS/STORM–GPS sensing of atmospheric water vapour for meteorology. *Journal of Atmospheric and Oceanic Technology*, *12*, 468–478. https://doi.org/10.1175/1520-0426(1995) 012<0468:GSOAWV>2.0.CO;2.

Saastamoinen, J. (1972). Atmospheric corrections for the troposphere and stratosphere in radio ranging of satellites. In S. W. Henriksen et al. (Eds.), *The use of artificial satellites for geodesy* (Monograph series) (Vol. 15, pp. 247–251). Washington DC: AGU.

Sánchez Arriola, J., Lindskog, M., Thorsteinsson, S., & Bojarova, J. (2016). Variational bias correction of GNSS ZTD in the HARMONIE modelling system. *Journal of Applied Meteorology and Climatology, 55*, 1259–1276. https://doi.org/10.1175/JAMC-D-15-0137.1.

Schraff, C., Reich, H., Rhodin, A., Schomburg, A., Stephan, K., Periáñez, A., & Potthast, R. (2016). Kilometre-scale ensemble data assimilation for the COSMO model (KENDA). *Quarterly Journal of the Royal Meteorological Society, 142*(696), 1453–1472.

Seidel, D. J., Ao, C. O., & Li, K. (2010). Estimating climatological planetary boundary layer heights from radiosonde observations: Comparison of methods and uncertainty analysis. *Journal of Geophysical Research Atmospheres, 115*(D16).

Smet, G., Termonia, P., & Deckmyn, A. (2012). Added economic value of limited area multi-EPS weather forecasting applications. *Tellus A, 64*, 18901.

Smith, E., & Weintraub, S. (1953, August), The constants in the equation for atmospheric refractive index at radio frequencies. *Proceedings of the IRE*, *41*(8), 1035–1037. https://doi.org/10.1109/JRPROC.1953.274297.

Smith, W., & Wessel, P. (1990, March). Gridding with continuous curvature splines in tension. *Geophysics*, *55*(3), 293–305. https://doi.org/10.1190/1.1442837.

Stephan, K., Klink, S., & Schraff, C. (2008). Assimilation of radar-derived rain rates into the convective-scale model COSMO-DE at DWD. *Quarterly Journal of the Royal Meteorological Society, 134*(634), 1315–1326.

Stoev, K., & Guerova, G. (2017). Climatology of the foehn in Sofia for 1975–2014. *International Journal of Climatology*. In review 9/2017. http://suada.phys.uni-sofia.bg/?page_id=3801

Stoycheva, A., & Guerova, G. (2015). Study of fog in Bulgaria by using the GNSS tropospheric products and large scale dynamic analysis. *Journal of Atmospheric and Solar-Terrestrial Physics, 133*, 87–97. https://doi.org/10.1016/j.jastp.2015.08.004.

Stoycheva, A., Manafov, I., Vassileva, K., & Guerova, G. (2017). Study of persistent fog in Bulgaria with Sofi a Stability Index, GNSS tropospheric products and WRF simulations. *Journal of Atmospheric and Solar-Terrestrial Physics, 161*, 160–169. https://doi.org/10.1016/j.jastp.2017.06.011.

Stull, R. (1995). *Meteorology today for scientists and engineers* (385 p). Minneapolis: West Publishing.

Van Malderen, R., Brenot, H., Pottiaux, E., Beirle, S., Hermans, C., De Mazière, M., Wagner, T., De Backer, H., & Bruyninx, C. (2014). A multi-site techniques intercomparison of integrated water vapour observations for climate change analysis. *Atmospheric Measurement Techniques Discussions, 7*, 1075–1151. https://doi.org/10.5194/amtd-7-1075-2014.

Vedel, H., Huang, X. Y., Haase, J., Ge, M., & Calais, E. (2004). Impact of GPS Zenith tropospheric delay data on precipitation forecasts in Mediterranean France and Spain. *Geophysical Research Letters, 31*(2), 2004.

Vey, S., Dietrich, R., Fritsche, M., Rülke, A., Steigenberger, P., & Rothacher, M. (2009, May). On the homogeneity and interpretation of precipitable water time series derived from global GPS observations. *Journal of Geophysical Research Atmospheres*, *114*(D10). https://doi.org/10.1029/2008JD010415.

Wang, J., Zhang, L., & Dai, A. (2005). Global estimates of water-vapour-weighted mean temper-ature of the atmosphere for GPS applications. *Journal Geophysical Research, 110*, D21101. https://doi.org/10.1029/2005JD006215.

Wang, J., Zhang, L., Dai, A., van Hove, T., & van Baelen, J. (2007, June). A near-global, 2-hourly data set of atmospheric precipitable water from ground-based GPS measurements. *Journal of Geophysical Research Atmospheres*, *112*(D11). https://doi.org/10.1029/2006JD007529.

Wang, X., Barker, Snyder, C., & Hamill, T. M. (2008). A hybrid ETKF–3DVAR data assimilation scheme for the WRF Model. Part I: Observing system simulation experiment. *Monthly Weather Review, 136*, 5116–5131.

Watson, D. (1982). Acord: Automatic contouring of raw data. *Computers and Geosciences, 8*(1), 97–101. https://doi.org/10.1016/0098-3004(82)90039-5.

Wattrelot, E., Caumont, O., & Mahfouf, J. F. (2014). Operational implementation of the 1D+ 3D-Var assimilation method of radar reflectivity data in the AROME model. *Monthly Weather Review, 142*(5), 1852–1873.

Yan, X., Ducrocq, V., Poli, P., Jaubert, G., & Walpersdorf, A. (2008). Mesoscale GPS Zenith delay assimilation during a Mediterranean heavy precipitation event. *Advances in Geosciences, 17*, 71–77.

Yan, X., Ducrocq, V., Poli, P., Hakam, M., Jaubert, G., & Walpersdorf, A. (2009). Impact of GPS zenith delay assimilation on convective-scale prediction of Mediterranean heavy rainfall. *Journal of Geophysical Research, 114*(D03104), 2009.

Zus, F., Bender, M., Deng, Z., Dick, G., Heise, S., Shang-Guan, M., & Wickert, J. (2012). A methodology to compute GPS slant total delays in a numerical weather model. *Radio Science, 47*, RS2018.

Zus, F., Dick, G., Heise, S., & Wickert, J. (2014). A forward operator and its adjoint for GPS slant total delays. *Radio Science, 50*(5), 393–405.